

On the Segregation of Dark Matter Substructure

Frank C. van den Bosch^{1*}, Fangzhou Jiang¹, Duncan Campbell¹, Peter Behroozi²

¹*Department of Astronomy, Yale University, P.O. Box 208101, New Haven, CT 06520-8101*

²*Space Telescope Science Institute, Baltimore, MD 21218, USA*

ABSTRACT

We present the first comprehensive analysis of the segregation of dark matter subhaloes in their host haloes. Using three different numerical simulations, and two different segregation strength indicators, we examine the segregation of twelve different subhalo properties with respect to both orbital energy and halo-centric radius (in real space as well as in projection). Subhaloes are strongly segregated by accretion redshift, which is an outcome of the inside-out assembly of their host haloes. Since subhaloes that were accreted earlier have experienced more tidal stripping, subhaloes that have lost a larger fraction of their mass at infall are on more bound orbits. Subhaloes are also strongly segregated in their masses and maximum circular velocities at accretion. We demonstrate that part of this segregation is already imprinted in the infall conditions. For massive subhaloes it is subsequently boosted by dynamical friction, but only during their first radial orbit. The impact of these two effects is counterbalanced, though, by the fact that subhaloes with larger accretion masses are accreted later. Because of tidal stripping, subhaloes reveal little to no segregation by present-day mass or maximum circular velocity, while the corresponding torques cause subhaloes on more bound orbits to have smaller spin. There is a weak tendency for subhaloes that formed earlier to be segregated towards the center of their host halo, which is an indirect consequence of the fact that (sub)halo formation time is correlated with other, strongly segregated properties. We discuss the implications of our results for the segregation of satellite galaxies in galaxy groups and clusters.

Key words: methods: analytical — methods: statistical — galaxies: formation — galaxies: haloes — galaxies: kinematics and dynamics — cosmology: dark matter

1 INTRODUCTION

It is well established that galaxy groups and clusters reveal segregation of their member galaxies. In particular, early-type galaxies (red, passive, elliptical) follow a more centrally concentrated radial distribution (and have a narrower line-of-sight velocity distribution) than their late-type (blue, active, spiral) counterparts (e.g. Postman & Geller 1984; Whitmore, Gilmore & Jones 1993; Biviano et al. 1996, 2002; Carlberg et al. 1997; Balogh et al. 2000, 2004; Domínguez et al. 2002; Girardi et al. 2003; Gómez et al. 2003; Goto et al. 2003, 2004; Lares, Lambas & Sánchez 2004; Weinmann et al. 2006; Blanton & Berlind 2007; van den Bosch et al. 2008; Wetzel, Tinker & Conroy 2012). In addition, numerous studies have detected luminosity and/or stellar mass segregation in the sense that more luminous and massive galaxies are located at smaller group- or cluster-centric distances (e.g., Rood & Turnrose 1968; Quintana 1979; den Hartog & Katgert 1996; Adami, Biviano & Mazure 1998; Bi-

viano et al. 2002; Lares, Lambas & Sánchez 2004; McIntosh et al. 2005; van den Bosch et al. 2008; Presotto et al. 2012; Balogh et al. 2014; Roberts et al. 2015). However, it is important to point out that the presence of luminosity and/or stellar mass segregation in groups and clusters is still contentious (see e.g., Pracy et al. 2005; Hudson et al. 2010; von der Linden et al. 2010; Wetzel et al. 2012; Ziparo et al. 2013; Vulcani et al. 2013).

What is the origin of this segregation? It is useful to distinguish the following two options. Segregation can arise as a manifestation of the environmental impact of galaxy evolution. In this case, the evolution of a satellite galaxy is directly (and causally) influenced by its actual location (or orbit) in the dark matter halo of its host. An example is ram-pressure stripping, which can cause a satellite galaxy to quench its star formation. For ram-pressure to be effective, the satellite needs to be moving relatively fast, through a relatively dense gaseous atmosphere, which selects out orbits with a small pericentric distance. Alternatively, segregation can also have its origin in the dark sector, combined with the fact that galaxy properties are tightly correlated with

* E-mail: frank.vandenbosch@yale.edu

(sub)halo properties such as mass. In this picture, there is segregation of dark matter subhaloes according to one or more of their properties, while the galaxy properties are determined by the pre-infall properties of their dark matter haloes. An example is dynamical friction, which causes the segregation of more massive subhaloes towards the center of the host halo. If more massive subhaloes host more luminous galaxies, as expected, luminosity segregation would be a natural outcome. The main difference between these two scenarios is whether the relevant galaxy property (i.e., the property that reveals segregation) is determined pre- or post-infall. Although it is useful to make this distinction, we emphasize that these two ‘scenarios’ are not mutually exclusive.

The origin of the segregation by galaxy type (color, star formation rate, morphology) is most commonly linked to an environmental impact of galaxy evolution, even though it is still heavily debated which physical processes dominate the quenching and/or morphological transformation of satellite galaxies. It is important, though, to realize that this is not the only explanation. In fact, one can also explain segregation by galaxy type as a manifestation of segregation in the dark sector. This was nicely demonstrated in Watson et al. (2015), who showed that simply linking the star formation rate (hereafter SFR) of a (satellite) galaxy to the formation time of its dark matter halo, a procedure dubbed ‘age-matching’ (Hearin & Watson 2013; Hearin et al. 2014), can accurately reproduce the difference in the radial distributions of quenched and active satellite galaxies in host haloes that span several orders of magnitude in mass. This suggests that dark matter subhaloes are somehow segregated by formation time, and that this segregation is sufficient to explain the segregation by SFR of their associated satellite galaxies.

The origin of luminosity segregation is most commonly linked to dynamical friction, which implies that it has its origin in the dark sector. However, this picture is complicated by the fact that dark matter subhaloes experience tidal mass loss. Although more massive subhaloes experience stronger dynamical friction, which causes them to segregate out to smaller halo-centric distances, this also enhances their mass loss rate, which in turn makes them less susceptible to dynamical friction. Because of this tug of war between dynamical friction and tidal mass stripping, it is difficult to predict a priori whether and how subhaloes are segregated by mass.

It is clear from the discussion above that understanding the origin of segregation requires a detailed study as to how dark matter subhaloes are segregated. In particular, in this day and age of linking galaxy properties to dark matter properties, understanding segregation in the dark sector is of paramount importance for understanding small-scale clustering. Although there is no shortage of papers that have used numerical simulations to study the statistics and properties of dark matter subhaloes, there has been relatively little focus on how subhaloes are segregated. Regarding mass segregation, simulations have produced mixed results: whereas several authors find more massive subhaloes to be *less* centrally concentrated in terms of their radial distribution in the host halo (De Lucia et al. 2004; Reed et al. 2005; Angulo et al. 2009; Contini, De Lucia & Borgani 2012), there are also reports of no (significant) segregation by mass (Diemand, Moore & Stadel 2004; Springel

et al. 2008; Ludlow et al. 2009), or of a weak segregation in the opposite sense (Gao et al. 2004). Several studies have pointed out that subhaloes selected based on their mass (or maximum circular velocity) *at accretion* are more centrally concentrated than those selected based on their present-day mass or velocity (Gao et al. 2004; Nagai & Kravtsov 2005; Kuhlen, Diemand & Madau 2007; Ludlow et al. 2009; Contini et al. 2012), although none of these studies has investigated this in any detail. In terms of properties other than mass, Gao et al. (2004), Faltenbacher & Diemand (2006) and Contini et al. (2012) have shown that subhaloes that were accreted later are located at larger halo-centric radii, Wu et al. (2013) find that subhaloes with larger maximum circular velocities are segregated towards the center of their host halo, while Reed et al. (2005) and Onions et al. (2013) find subhaloes at smaller halo-centric radii to have lower spin.

This paper presents the first comprehensive study of the segregation of dark matter subhaloes in numerical simulations. In particular, we study the segregation of 12 different subhalo properties with respect to both halo-centric radius (in real space as well as in projection) and orbital energy. We compare the results from three different simulations run with two different N -body codes, quantify segregation strength using two different indicators, and carefully analyze the origin of the various forms of segregation we identify. There are three ‘mechanisms’ than can give rise to segregation of subhaloes. The most well-known is two-body relaxation, which drives the system towards equipartition, and thus segregation by mass. In the case of subhaloes, this two-body relaxation manifests itself in the form of dynamical friction. Segregation may also arise from the fact that dark matter haloes assemble from the inside out. As a consequence, subhaloes that were accreted earlier, when the main progenitor of the present day host halo was smaller, typically end up at smaller halo-centric distances. Any subhalo property that is correlated with accretion time is therefore likely to show some amount of segregation. And finally, it may be the case that there are correlations between some subhalo properties and their orbital properties at accretion. In particular, if subhalo property P is correlated with the orbital energy at infall, segregation with respect to property P will have been imprinted *at accretion*. In addition to these three ‘primary’ mechanisms, segregation can also have an indirect origin, and simply arise from a correlation with another property that is physically segregated. In this paper we will investigate which subhalo properties are segregated and with what strength, and we will also examine which of the various mechanisms discussed above is responsible for this segregation. In a forthcoming paper (Lu et al., in preparation), we use this knowledge combined with the observed segregation of galaxy properties such as luminosity, stellar mass, color and star formation rate, to put constraints on the galaxy-dark matter connection and on the various physical processes related to galaxy formation and evolution.

This paper is organized as follows. §2 describes the numerical simulations used, the selection of our sample of subhaloes, the various segregation properties and indicators, as well as the two statistics we use to gauge segregation strength. Results on the segregation of our 12 subhalo properties are presented in §3, while their origin is discussed in §4. We summarize and discuss our results in §5.

Table 1. Numerical Simulations used in this Paper

Simulation (1)	$\Omega_{m,0}$ (2)	$\Omega_{\Lambda,0}$ (3)	$\Omega_{b,0}$ (4)	σ_8 (5)	n_s (6)	h (7)	L_{box} (8)	N_p (9)	m_p (10)	Reference (11)
Bolshoi	0.270	0.730	0.047	0.82	0.95	0.70	250	2048 ³	1.35×10^8	Klypin et al. (2011)
Chin250	0.286	0.714	0.047	0.82	0.96	0.70	250	2048 ³	1.44×10^8	Becker et al. (in prep.)
Chin400	0.286	0.714	0.047	0.82	0.96	0.70	400	2048 ³	5.91×10^8	Becker et al. (in prep.)

Parameters of the various numerical simulations used in this paper. Columns (2) - (7) list the present-day cosmological density parameters for the matter, $\Omega_{m,0}$, the cosmological constant, $\Omega_{\Lambda,0}$, and the baryonic matter, $\Omega_{b,0}$, the normalization, σ_8 , and spectral index, n_s , of the matter power spectrum, and the Hubble parameter, $h = H_0/(100 \text{ km s}^{-1} \text{ Mpc}^{-1})$. Columns (8) - (10) list the box size of the simulation, L_{box} , (in $h^{-1} \text{ Mpc}$), the number of particles used, N_p , and the particle mass, m_p (in $h^{-1} M_{\odot}$), respectively. More details regarding each simulation can be found in the references listed in Column (11).

2 METHODOLOGY

This section describes the numerical simulations, the selection of subhaloes, and the method used to assess their segregation. However, we start with a brief introduction of halo basics, outlining a number of definitions and notations.

2.1 Halo Basics and Notation

Throughout this paper we distinguish between dark matter host haloes and dark matter subhaloes. The latter have their center located inside the virial radius of a host halo. Host haloes at redshift z are defined as spherical systems with a virial radius r_{vir} inside of which the average density is equal to $\Delta_{\text{vir}}(z) \rho_{\text{crit}}(z)$. Here $\rho_{\text{crit}}(z) = 3H^2(z)/8\pi G$ is the critical density for closure, and

$$\Delta_{\text{vir}}(z) = 18\pi^2 + 82x - 39x^2 \quad (1)$$

with $x = \Omega_m(z) - 1$ (Bryan & Norman 1998). The (virial) mass of a host halo is defined as the mass within the virial radius r_{vir} and indicated by M . Subhaloes are defined as haloes whose center falls inside the virial radius of a (more massive) host halo, and their mass, indicated by m , is defined as the sum of the masses of the particles that are deemed bound to the subhalo by the subhalo finder used (see below).

Throughout this paper, we approximate that host haloes follow an NFW density profile (Navarro, Frenk & White 1997), for which the gravitational potential is given by

$$\Phi(r) = -V_{\text{vir}}^2 \frac{\ln(1+cx)}{f(c)x} = -\left(\frac{V_{\text{max}}}{0.465}\right)^2 \frac{\ln(1+cx)}{cx}. \quad (2)$$

Here $V_{\text{vir}} = \sqrt{GM/r_{\text{vir}}}$ is the circular velocity at the virial radius, $x = r/r_{\text{vir}}$,

$$f(x) = \ln(1+x) - \frac{x}{1+x}, \quad (3)$$

and c is the halo's concentration parameter. The central potential of an NFW halo is given by

$$\Phi_0 \equiv \Phi(0) = -\left(\frac{V_{\text{max}}}{0.465}\right)^2. \quad (4)$$

where V_{max} is the maximum circular velocity, which for an NFW profile is given by

$$V_{\text{max}} = 0.465 V_{\text{vir}} \sqrt{\frac{c}{f(c)}}, \quad (5)$$

We will use Φ_0 throughout to normalize the orbital energy of subhaloes.

Finally, the (dimensionless) spin parameter of a dark matter (sub)halo of mass M is defined as

$$\lambda \equiv \frac{J|E|^{1/2}}{GM^{5/2}}, \quad (6)$$

(Peebles 1969). Here J is the total angular momentum of the halo, G is the gravitational constant, and $E = T + U$ is the total energy, with T and U the total kinetic and potential energies, respectively.

2.2 Numerical Simulation

In this paper we use three cosmological N -body simulations to study the segregation of dark matter subhaloes: the ‘Bolshoi’ simulation (Klypin, Trujillo-Gomez & Primack 2011), and two simulations (‘Chin250’ and ‘Chin400’) of the Chinchilla suite (Becker et al., in prep.). The cosmological parameters of the Bolshoi and Chinchilla simulations (see Table 1) are slightly different, but both are consistent with the latest constraints from the Planck satellite (Planck Collaboration 2015). Bolshoi has been run with the Adaptive Refinement Tree (ART) code (Kravtsov, Klypin & Khokhlov 1997), while the Chinchilla simulations have been run using Gadget-2 (Springel 2005). All simulations follow the evolution of 2048³ dark matter particles in a periodic simulation box. The box sizes and particle masses of the simulations are listed in Table 1.

For all three simulations we use the $z = 0$ halo catalogs obtained with the phase-space halo finder ROCKSTAR (Behroozi et al. 2013a,b), which uses adaptive, hierarchical refinement of friends-of-friends groups in six phase-space dimensions and one time dimension. As demonstrated in Knebe et al. (2011, 2013), this results in a very robust tracking of (sub)haloes (see also van den Bosch & Jiang 2014). In line with the halo definition given above, ROCKSTAR host haloes are defined as spheres with an average density equal to $\Delta_{\text{vir}}\rho_{\text{crit}}$. Subhaloes are defined as haloes whose center lies within the virial radius, r_{vir} , of a bigger halo.

2.3 Sample Selection

When investigating the segregation of dark matter subhaloes in numerical simulations, it is important to select your sam-

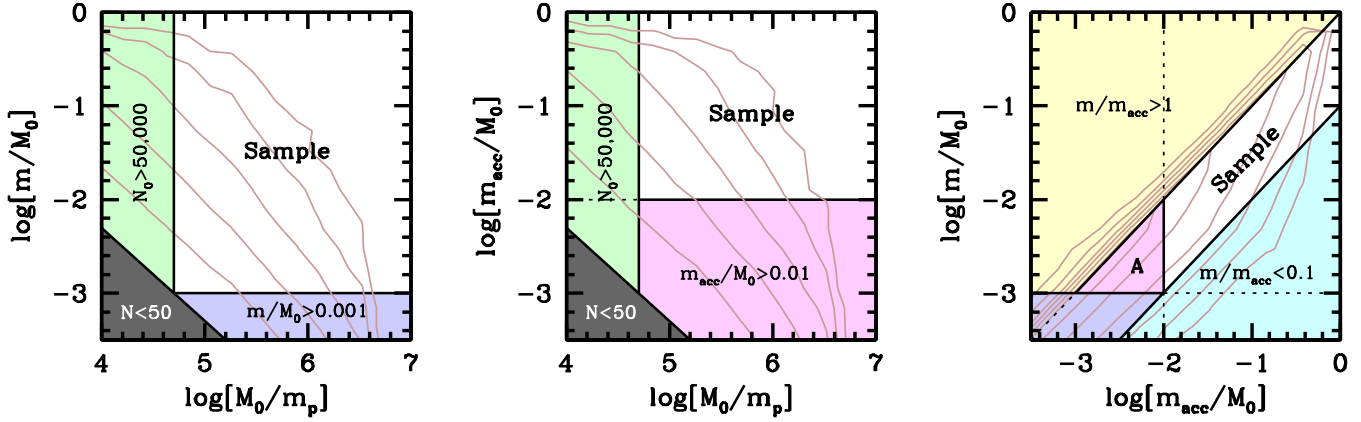


Figure 1. Illustration of the various criteria used for the selection of our sample of subhaloes. From left to right the panels plot $\log[m/M_0]$ vs. $\log[M_0/m_p]$, $\log[m_{\text{acc}}/M_0]$ vs. $\log[M_0/m_p]$, and $\log[m/M_0]$ vs. $\log[m_{\text{acc}}/M_0]$. The white region, labeled ‘Sample’ indicates the region in (M_0, m, m_{acc}) -parameter space occupied by subhaloes in our fiducial sample. Color shaded regions reflect the various cuts discussed in the text, while contours indicate the number density of subhaloes in the Bolshoi simulation. The triangular, pink-shaded region labeled ‘A’ indicates the region in (M_0, m, m_{acc}) -parameter space that is added to our sample if we remove the constraint that $m_{\text{acc}}/M_0 \geq 0.01$. The impact of adding these subhaloes to our sample is discussed throughout the text and in Appendix A. Note that we deliberately refrained from using primary colors in order to avoid a too close resemblance with the copyrighted art by Piet Mondrian.

ple carefully. Fig. 1 illustrates the various selection criteria we have applied to the host haloes and subhaloes in our three simulation boxes. First off, throughout we limit our study to subhaloes with at least 50 particles, which is roughly the limit below which resolution effects start to affect completeness in the subhalo mass function (van den Bosch & Jiang 2014). The dark-grey triangular region in the left-hand panel of Fig. 1 show the constraints this puts on the ratio of the present-day subhalo mass, m , to that of its host halo, M_0 , as a function of M_0/m_p , where m_p is the simulation particle mass. As a compromise between sample size and dynamical range, we first construct a complete sample of all subhaloes with $\log[m/M_0] \geq -3$, which excludes the purple-shaded region in Fig. 1. Having the sample be complete implies that we restrict ourselves to host haloes with at least 50,000 particles, which excludes the green-shaded regions in Fig. 1. This constraint on host halo mass translates to $M_0 > 6.75 \times 10^{12} h^{-1} M_\odot$ for the Bolshoi simulation, while the equivalent lower limits for the Chin250 and Chin400 simulations are $7.20 \times 10^{12} h^{-1} M_\odot$ and $2.96 \times 10^{13} h^{-1} M_\odot$, respectively.

In addition to these constraints on m and M_0 , we also select our subhaloes based on their mass at accretion, m_{acc} . Since one typically expects a subhalo to loose mass after accretion, due to tidal stripping by the host halo, we demand that $m/m_{\text{acc}} \leq 1$, excluding the yellow-shaded region in the right-hand panel. This only removes $\sim 5\%$ of the subhaloes, most of which have a present day subhalo mass just slightly larger than unity. We also exclude subhaloes that have lost more than 90 percent of their mass, which excludes the cyan-shaded region in the right-hand panel of Fig. 1. We emphasize that removing these two constraints on m/m_{acc} (while keeping all other constraints intact) only increases the sample size by $\sim 13\%$, and has no discernible impact on any of the results presented below. We mainly use these criteria to have a sharper defined sample.

Finally, we also impose that $\log[m_{\text{acc}}/M_0] \geq -2$, which excludes the pink-shaded regions in Fig. 1. This is done to have a sample of subhaloes that is more reminiscent of what

observers may use to study segregation in galaxy groups and clusters. After all, the luminosities and stellar masses of satellite galaxies are believed to be tightly correlated with the corresponding subhalo masses *at accretion*, which is the premise of the succesful and popular subhalo abundance matching technique (e.g., Vale & Ostriker 2006; Conroy, Wechsler & Kravtsov 2006; Behroozi, Conroy & Wechsler 2010). This cut in m_{acc}/M_0 severely reduces the sample size, by about a factor four. In particular, in the right-hand panel of Fig. 1 there are roughly three times as many subhaloes in the pink, triangular region (marked ‘A’) than in the white region demarcating our fiducial sample. As we discuss in detail in Appendix A, adding these galaxies to our sample (i.e., removing the constraint that $\log[m_{\text{acc}}/M_0] \geq -2$) has a strong impact on the segregation of subhaloes by present-day mass (see also §3.1 and §4.7).

In addition to the constraints on M_0 , m , and m_{acc} , we also remove all subhaloes ($\sim 2.7\%$) for which the virial ratio $T/|U| > 1$ (see §2.4 below for a definition). These latter are subhaloes that are very far from virial equilibrium, and for which masses and circular velocities are extremely uncertain. We emphasize, though, that this restriction again has no significant impact on any of our results. Finally, we remove all subhaloes ($\sim 1.1\%$) whose orbital energy $E > 0$, and which are thus not bound to their host. For each of the three simulation boxes, this yields samples of $\sim 22,000$ subhaloes, for a grand total of 66,401 subhaloes in all three simulation boxes combined.

We acknowledge that these selection criteria are somewhat arbitrary, and depending on the scientific question at hand, one might prefer to apply other selection criteria. We have experimented with different samples, and found most results to be remarkably robust, at least in a qualitative way. In those cases where this is *not* the case, we will mention so explicitly in the text.

Table 2. Segregation Properties

m	the present-day mass of the subhalo
m_{acc}	the mass of the subhalo at accretion
m_{peak}	the peak mass of the subhalo, defined as the maximum mass it ever had along its entire history.
m/m_{acc}	the ratio of the present-day subhalo mass to that at accretion
V_{max}	the maximum circular velocity of the present-day subhalo
V_{acc}	the value of V_{max} of the subhalo at accretion
V_{peak}	the peak value of V_{max} along the halo's history
$V_{\text{max}}/V_{\text{acc}}$	the ratio of present-day V_{max} to that at accretion
z_{acc}	the subhalo's redshift of accretion
z_{form}	the subhalo's formation redshift, defined as redshift at which main progenitor reaches mass equal to $m_{\text{peak}}/2$
λ	the present-day spin parameter of the subhalo, as defined by Eq. (6)
$T/ U $	the virial parameter, with T and U the total kinetic and potential energy of the subhalo

2.4 Segregation Properties and Indicators

The main goal of this paper is to investigate how dark matter subhaloes are segregated. Although segregation is most often discussed in terms of radial segregation by mass (i.e., more massive objects are located at smaller radii), in this paper we take a more comprehensive approach, and examine the segregation of a wide variety of subhalo properties; not just mass. We differentiate between *segregation indicators*, such as radius or binding energy, which express a relation between the subhalo and its host halo, and *segregation properties*, such as mass or spin parameter, which are (mainly internal) properties of the subhalo. The goal of this study is to investigate which of the segregation properties are most segregated, and how this segregation manifests itself as function of the different segregation indicators.

We consider the following segregation indicators:

- r/r_{vir} the three-dimensional distance between the center of the subhalo and the center of its host halo, normalized by the virial radius of the host halo.
- R/R_{vir} the two-dimensional, projected distance between the center of the subhalo and the center of its host halo, normalized by the virial radius of the host halo. Throughout, we compute R by simply projecting all haloes and subhaloes along the z -direction of the simulation box.
- $E/|\Phi_0|$ the (specific) orbital energy of the subhalo, normalized by the value of the host halo's gravitational, central potential.

The specific orbital energy is computed as $E = v^2/2 + \Phi(r)$, where

$$v = \frac{M_0}{M_0 + m} |\vec{v}_{\text{host}} - \vec{v}_{\text{sub}}| \quad (7)$$

is the speed of the subhalo with respect to the center of mass of the host+subhalo system (here \vec{v}_{host} and \vec{v}_{sub} are the velocities of host halo and subhalo with respect to the simulation box), and $\Phi(r)$ is the potential energy at the location r of the subhalo. We compute the latter using Eq. (2) assuming that the host halo is a spherical NFW halo with a concentration parameter, c , that we extract from the halo catalog. Bound orbits have $-1 \leq E/|\Phi_0| < 0$, with more negative values indicating a more bound orbit. Clearly, $E/|\Phi_0|$ is the most physical segregation indicator, whereas R/R_{vir} is the one that is most easily accessible observationally. We emphasize that, when using R/R_{vir} , we still only consider true

subhaloes that are located within the (3D) virial radius of the host. The impact of interlopers is beyond the scope of this paper, but will be addressed in detail in a follow-up paper in which we compare our findings to observations (Lu et al., in preparation).

In addition to these three segregation indicators, we consider the twelve segregation properties listed in Table 2. Throughout we normalize the subhalo masses m , m_{acc} and m_{peak} by the mass, M_0 , of the present day host halo, and the subhalo velocities V_{max} , V_{acc} , and V_{peak} by the virial velocity, $V_{\text{vir},0}$, of the present-day host halo. The subhalo's accretion redshift, z_{acc} , is defined as the *last* epoch at which the subhalo entered the virial radius of its present-day host, while the formation redshift, z_{form} , is defined as the *first* epoch at which the subhalo's main progenitor reaches a mass equal to, or larger than, $m_{\text{peak}}/2$. Finally, regarding the virial ratio $T/|U|$, we emphasize that we have ignored any external potential (e.g., such as that from the host halo) when computing the potential energy, U , of the subhaloes. If the subhalo is in isolation and in virial equilibrium with negligible surface pressure, then we expect that $T/|U| = 1/2$ (see e.g., § 5.4.4 in Mo et al. 2010).

2.5 Quantifying Segregation Strength

For each combination of segregation property, P , and segregation indicator, S , we compute the Spearman rank-order correlation coefficient, r_s , as an indicator of the segregation strength. We have experimented with a number of alternative indicators, including Kendall's tau and Pearson's linear correlation coefficient, which always gave results in good, qualitative agreement[†] with those based on r_s . No segregation corresponds to $r_s = 0$, while positive (negative) values of r_s indicate that P is positively (negatively) correlated with S (i.e., we say that subhalo property P reveals segregation with respect to indicator S). In order to gauge the significance of a non-zero r_s , we compute r_s for 1000 Monte-Carlo samples in which we reshuffle the rank-orders of P , while keeping the rank-orders of S fixed. By construction, these shuffled samples have no segregation (i.e., no rank-order correlation), and the standard deviation of r_s among

[†] Typically, Pearson's linear correlation coefficient agrees with r_s to better than 15%.

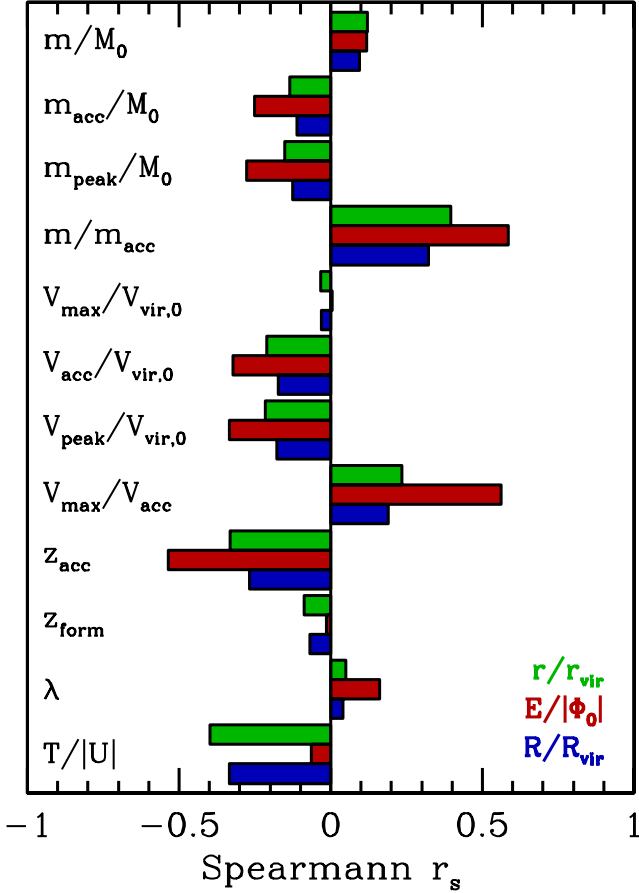


Figure 2. Bar graph depicting the values of the Spearman rank-order correlation coefficient, r_s , for the twelve subhalo properties (as indicated) with respect to r/r_{vir} (green bars), $E/|\Phi_0|$ (red bars) and R/R_{vir} (blue bars).

those 1000 values, σ_r , is indicative of the variance in r_s that one can obtain in the absence of segregation. Since r_s is non-parametric, σ_r only depends on the number of subhaloes, and is independent of P and S . For the sample of subhaloes used here, we find that $\sigma_r = 0.0040$, indicating that a value of $|r_s| > 0.012$ corresponds to a significant rank-order correlation between P and S at 99.9% confidence.

In addition to r_s , which is non-parametric, we also quantify the segregation strength using the parameter

$$\mathcal{R} \equiv \frac{\langle P \rangle_{0-25}}{\langle P \rangle_{75-100}}, \quad (8)$$

where $\langle P \rangle_{0-25}$ and $\langle P \rangle_{75-100}$ are the averages of P_i for the quartiles of subhaloes with the lowest and highest values of S_i , respectively. If $\mathcal{R} > 1$ (< 1) it indicates that subhaloes in the lower quartile of S_i have a property P that is \mathcal{R} times larger (smaller) than for the subhaloes in the upper quartile of S_i . The advantage of \mathcal{R} is that it is easier to interpret, whereas r_s better expresses the statistical significance of the segregation. We caution, though, that r_s is only a meaningful segregation strength indicator if the correlation between P and S is monotonic. As we show below, this is not always the case.

3 RESULTS

As indicated in §2.4 we have a total of 12 subhalo properties, P , and three segregation indicators, S . The values of r_s and \mathcal{R} , for all 36 combinations of segregation indicator and property, are listed in Table 3. Note that *all* twelve subhalo properties are significantly segregated (in that $|r_s| > 0.012$) with respect to *each* of the three segregation indicators, but for one exception: $V_{\text{max}}/V_{\text{vir},0}$, the present-day maximum circular velocity of subhaloes, normalized by the virial velocity of the host halo, is the only subhalo property that is consistent with having no significant correlation with orbital binding energy.

As a visualization of these results, the bar graph in Fig. 2 shows the Spearman rank-order correlation coefficients for all twelve subhalo properties, with green, red and blue bars indicating the value of r_s with respect to r/r_{vir} , $E/|\Phi_0|$, and R/R_{vir} , respectively. A few trends are immediately evident. As expected, segregation with respect to the projected radius R/R_{vir} is always weaker than with respect to the 3D radius, but only by a little bit. In particular, the value of $|r_s|$ in projection is typically 20% smaller than that in 3D, while the difference is even smaller for the \mathcal{R} parameter. In virtually all cases, the absolute value of r_s is largest when using $E/|\Phi_0|$ as indicator, which is what one expects if the segregation is physical. Two notable outliers in this respect are $T/|U|$ and z_{form} . The virial ratio in particular shows strong segregation (large values of $|r_s|$) when using r/r_{vir} or R/R_{vir} as indicators, but has one of the smallest values for $|r_s|$ when using $E/|\Phi_0|$ as segregation indicator. As we discuss in §4.1 below, this is a consequence of impulsive heating at peri-centric passage.

Next we proceed as follows. For a given set of S and P , we first rank-order the subhaloes by their segregation indicator S . Next we split the rank-ordered sample in 40 equal-number bins, and compute, for each bin, the averages of S and P . The results for 8 different segregation properties[‡], P , are indicated as open circles in Figs. 3 and 4. Different columns (rows) correspond to different segregation indicators (properties), and the corresponding value for r_s is indicated in the lower-left corner of each panel. Error bars indicate the range of segregation indicator for each bin. Different colors correspond to the three different simulation boxes, as indicated, and are typically in excellent mutual agreement. Plotting the medians of P , rather than the averages, yields plots that are virtually indistinguishable. In what follows we discuss some individual results in turn.

3.1 Masses and Circular Velocities

The first subhalo property we discuss is the mass ratio m/m_{acc} , whose correlation with respect to the three segregation indicators is indicated in the lower panels of Fig. 3. Clearly, m/m_{acc} is extremely strongly segregated, in the sense that subhaloes that have lost a larger fraction of their mass at accretion are on more bound orbits. This was first hinted at in the studies by Gao et al. (2004) and Nagai & Kravtsov (2005). Based on the \mathcal{R} statistic, the most bound

[‡] For the sake of brevity, we only show results for 8 out of 12 properties.

Table 3. Segregation Strength Indicators

Seg. Prop. (1)	Stat (2)	r/r_{vir} (3)	$E/ \Phi_0 $ (4)	R/R_{vir} (5)
m/M_0	r_s	0.120	0.118	0.095
	\mathcal{R}	1.058	1.416	1.058
m_{acc}/M_0	r_s	-0.136	-0.251	-0.112
	\mathcal{R}	1.644	2.643	1.537
m_{peak}/M_0	r_s	-0.151	-0.277	-0.125
	\mathcal{R}	1.687	2.821	1.573
m/m_{acc}	r_s	0.397	0.585	0.322
	\mathcal{R}	0.609	0.479	0.668
$V_{\text{max}}/V_{\text{vir},0}$	r_s	-0.034	0.005	-0.031
	\mathcal{R}	1.052	1.057	1.045
$V_{\text{acc}}/V_{\text{vir},0}$	r_s	-0.211	-0.321	-0.173
	\mathcal{R}	1.169	1.301	1.141
$V_{\text{peak}}/V_{\text{vir},0}$	r_s	-0.215	-0.335	-0.177
	\mathcal{R}	1.171	1.312	1.144
$V_{\text{max}}/V_{\text{acc}}$	r_s	0.235	0.561	0.189
	\mathcal{R}	0.904	0.810	0.920
z_{acc}	r_s	-0.332	-0.536	-0.268
	\mathcal{R}	2.119	3.131	1.862
z_{form}	r_s	-0.087	-0.014	-0.069
	\mathcal{R}	1.104	1.021	1.082
λ	r_s	0.050	0.161	0.040
	\mathcal{R}	0.927	0.798	0.938
$T/ U $	r_s	-0.399	-0.063	-0.335
	\mathcal{R}	1.207	1.043	1.174

For each segregation property (column 1), this table lists the values of the Spearman rank-order correlation coefficient, r_s , and the ratio \mathcal{R} defined by Eq. (8), for the segregation indicators r/r_{vir} (column 3), $E/|\Phi_0|$ (column 4), and R/R_{vir} (column 5).

quartile has, on average, lost more than two times as much mass than the least bound quartile, and with $r_s = 0.585$, the mass ratio m/m_{acc} is the subhalo property that reveals the strongest segregation among all 12 properties examined in this study. As we demonstrate in §4.5, this has its origin in the inside-out assembly of haloes combined with the impact of tidal stripping.

The second row of panels in Fig. 3 shows that subhaloes are also strongly segregated by m_{acc}/M_0 , to the extent that subhaloes that were more massive at accretion are on more bound orbits, and located at smaller halo-centric distances (see also Contini et al. 2012). The most bound quartile of subhaloes has accretion masses that are 2.6 times larger than for the least bound quartile. Results for m_{peak}/M_0 , shown in the third row of panels, are very similar to those for m_{acc}/M_0 . Based on the corresponding r_s and \mathcal{R} values, m_{peak} is slightly more segregated than m_{acc} , but only by a small amount. As we will demonstrate in §4.6, the segregation of m_{acc} and m_{peak} is a consequence of dynamical friction during the first orbital period, and is weakened by tidal disruption and by the fact that more massive subhaloes are typically accreted later.

The upper panels of Fig 3 show the results for the present-day mass, m , normalized by that of its host halo, M_0 . As it turns out, for this property it is difficult to discern a unique sign of segregation. Based on the values of r_s , which are positive for all three segregation indicators, more massive subhaloes are *less* bound and located at *larger* halo-

centric radii. Although in qualitative agreement with results from several other simulations (De Lucia et al. 2004; Reed et al. 2005; Angulo et al. 2009; Contini et al. 2012), this is opposite to naive expectations that more massive subhaloes should be more bound due to dynamical friction. As we will see below, this simple prediction is complicated by the fact that subhaloes experience appreciable amounts of mass loss. More confusing yet is the fact that the \mathcal{R} values for m/M_0 are larger than unity, indicating that the lower quartile of the r/r_{vir} and $E/|\Phi_0|$ distributions are actually *more massive* than the corresponding upper quartiles: this is opposite to the trend one seems to infer from the Spearman rank-order correlation coefficient. This apparent contradiction is explained by the fact that the trends of $\langle \log[m/M_0] \rangle$ with r/r_{vir} , $E/|\Phi_0|$ and R/R_{vir} are not monotonic.

In general, we find the results for the present-day halo mass to be extremely sensitive to sample selection. For example, if we were to include subhaloes with $-3 \leq \log[m_{\text{acc}}/M_0] < -2$ (i.e., we add subhaloes located in the pink-shaded, triangular region of the right-hand panel of Fig. 1), then the r_s values for all three segregation indicators become negative[§], and the equivalent of the upper panels of Fig. 3 now shows a monotonic decline of $\langle \log[m/M_0] \rangle$ with increasing r , E and R . Hence, *depending on the exact selection criteria used, subhaloes can reveal very different levels, and signs, of mass segregation*. The reason is, as we have already seen, that subhaloes are extremely strongly segregated in m/m_{acc} . As a consequence, if different sample selections make slightly different cuts in the distribution of m/m_{acc} , this can have strong impact on the results for m/M_0 (and also, albeit to a lesser extent, for m_{acc}/M_0). We also believe this to be the reason for a lack of consensus regarding the sign and strength of subhalo mass segregation in previous studies (see discussion in §1). Appendix A presents a more detailed, complementary description of the segregation of m/M_0 and m_{acc}/M_0 , together with a demonstration of the impact of sample selection.

Although not shown in Fig. 3, the results for V_{max} , V_{acc} , V_{peak} and $V_{\text{max}}/V_{\text{acc}}$ are qualitatively very similar to those for their corresponding mass indicators, m , m_{acc} , m_{peak} , and m/m_{acc} . Segregation is a bit stronger for $V_{\text{acc}}/V_{\text{vir},0}$ and $V_{\text{peak}}/V_{\text{vir},0}$ than for their respective masses. However, $V_{\text{max}}/V_{\text{vir},0}$ is the property with the overall weakest segregation among all 12 properties studies here. Note, though, that similar to m/M_0 , the segregation strength (and sign) of $V_{\text{max}}/V_{\text{vir},0}$ depends strongly on sample selection. We emphasize that a comparison of segregation strengths should be done based on the non-parametric r_s , and not \mathcal{R} . In fact, the \mathcal{R} values for the maximum circular velocities are closer to unity, in line with the expectations based on the fact that to reasonable approximation dark matter haloes have $V_{\text{max}} \propto M^{1/3}$.

3.2 Accretion Redshift, Formation Redshift, Spin Parameter and Virial Ratio

The upper panels of Fig. 4 show that subhaloes are also extremely strongly segregated by their redshift of accretion, z_{acc} . Subhaloes that were accreted earlier are more

[§] In the case of $E/|\Phi_0|$, r_s changes from 0.118 to -0.095 .

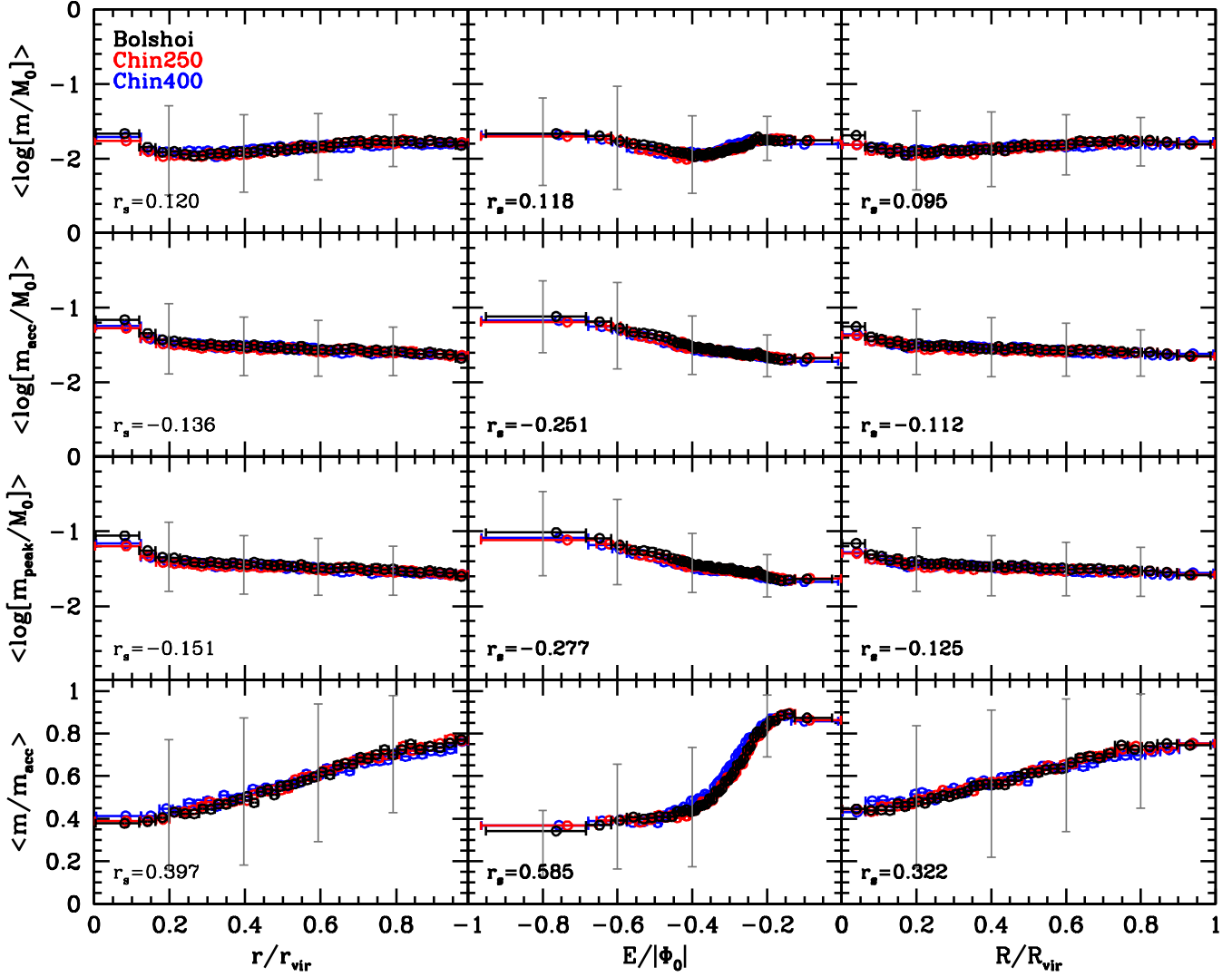


Figure 3. Each panel plots an average segregation property along the y-axis as function of a segregation indicator along the x-axis. The corresponding Spearman rank-order correlation coefficient is indicated in the lower-left corner of each panel, while different colors correspond to different simulation boxes, as indicated. From top to bottom the segregation properties are the present-day subhalo mass, $\log[m/M_0]$, the subhalo mass at accretion, $\log[m_{\text{acc}}/M_0]$, the peak subhalo mass $\log[m_{\text{peak}}/M_0]$ (all normalized by the present-day host halo mass, M_0), and the mass ratio m/m_{acc} . From left-to-right, the segregation indicators are the halo-centric distance, r/r_{vir} , the orbital energy, $E/|\Phi_0|$, and the projected halo-centric distance, R/R_{vir} . Horizontal errorbars indicate the width of each of the 40 bins used, which are chosen to have an equal number of subhaloes in them. Vertical errorbars indicate the 16 to 84 percentile range of the segregation properties; to avoid clutter, these are only plotted for four bins, and only for the Bolshoi simulation.

bound, and located at smaller halo-centric radii, in qualitative agreement with the results of Gao et al. (2004), Faltenbacher & Diemand (2006), and Contini et al. (2012). The fact that there is a small offset between the Chin250 and Chin400 results reflects the differences in host halo mass; since we only selected subhaloes in host haloes with at least 5×10^4 particles, the average host halo mass in the Chin400 simulation is somewhat larger than in the Chin250 (and Bolshoi) simulations. Since more massive haloes assemble later (e.g., van den Bosch 2002), the average accretion redshift of subhaloes in Chin400 is smaller than for Chin250. The small difference between the Chin250 and Bolshoi simulations, which have (almost) the same mass resolution, arises from the fact that Chin250 used fewer simulation outputs, causing a reduced temporal resolution of the halo merger

trees, which biases the accretion redshifts high. We find that the most bound quartile of subhaloes typically was accreted 2.5 to 3.0 Gyr earlier than the least bound quartile (for the range of host halo masses examined here). As we will see in §4.4, this segregation by accretion redshift is mainly a reflection of the inside-out assembly of dark matter haloes.

The second row of panels of Fig. 4 shows that the average formation redshift for the subhaloes in our sample is ~ 1.8 , and that z_{form} is weakly segregated in the sense that subhaloes that formed earlier are located further in, and on more bound orbits. The segregation is weak though, especially with respect to $E/|\Phi_0|$ for which $r_s = -0.014$ (one of the least significant Spearman correlation coefficient of all 36 listed in Table 3). Note also that, similar to present-

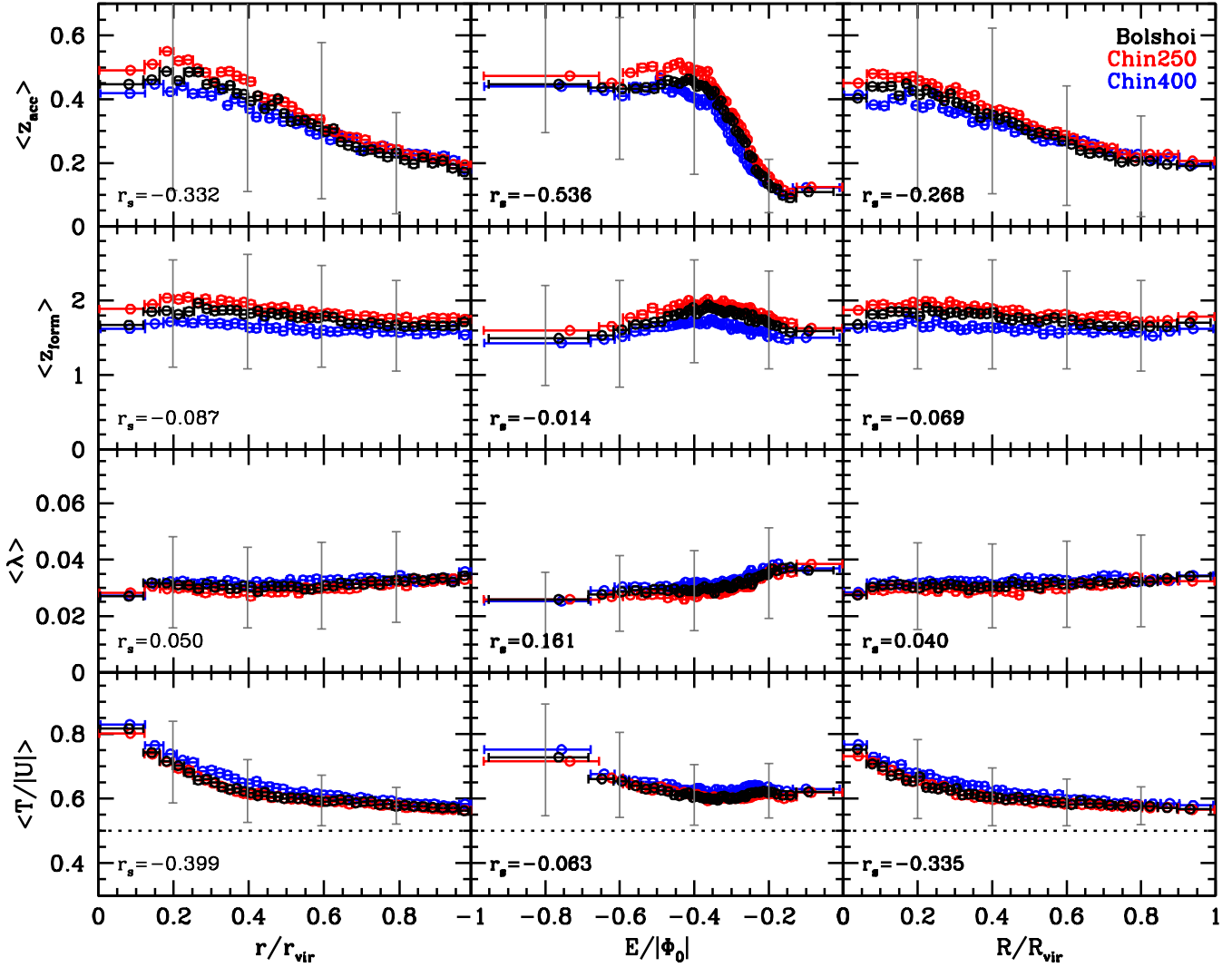


Figure 4. Same as Fig. 3, but for the subhalo accretion redshift z_{acc} (upper panels), the subhalo formation redshift z_{form} (second row of panels), the subhalo spin parameter λ (third row of panels), and the ratio of kinetic to potential energy, $T/|U|$ (lower panels). The dotted, horizontal lines in the lower panels correspond to virial equilibrium (i.e., $T/|U| = 1/2$).

day mass, the correlation between z_{form} and $E/|\Phi_0|$ is non-monotonic.

The third row of panels of Fig. 4 shows that the spin parameter of dark matter subhaloes (as defined by Eq. [6]) is only weakly segregated, in the sense that subhaloes on more bound orbits have somewhat lower λ . This is consistent with the findings of Reed et al. (2005) and Onions et al. (2013). As indicated by the \mathcal{R} value, the most bound quartile has a spin parameter that is $\sim 20\%$ smaller than for the least bound quartile. As discussed in §4.2, this segregation of spin parameters is a manifestation of the fact that more bound subhaloes have experienced more mass stripping (cf. lower panels of Fig. 3), and stronger tidal torques from their host.

Finally, the lower panels of Fig. 4 show the results for $T/|U|$. These show that the virial ratio is strongly segregated with respect to radius, in the sense that subhaloes at smaller halo-centric distances have $T/|U|$ ratios that deviate more from $1/2$, the value corresponding to virial equilibrium and indicated by horizontal, dotted lines. Although difficult to judge from Fig. 4, the r_s and \mathcal{R} values listed in Table 3

indicate that whereas $T/|U|$ is strongly segregated with respect to r/r_{vir} and R/R_{vir} , this is not the case with respect to $E/|\Phi_0|$. In fact, with $r_s = -0.063$ the rank-order correlation between the virial ratio and orbital energy is one of the weakest correlations among the ensemble of 36 listed.

4 THE ORIGIN OF SUBHALO SEGREGATION

In the previous section we described how each of the twelve subhalo properties is segregated with respect to each of the three segregation indicators. We now turn to address the origin of this segregation. We will do so roughly in the reverse order in which we presented the results in the previous section, starting with the segregation of the virial ratio, $T/|U|$. We will not discuss the velocity-based properties $V_{\text{max}}/V_{\text{vir},0}$, $V_{\text{acc}}/V_{\text{vir},0}$, $V_{\text{peak}}/V_{\text{vir},0}$ and $V_{\text{max}}/V_{\text{vir},0}$, but note that their segregation origin is akin to that of their corresponding mass-based property.

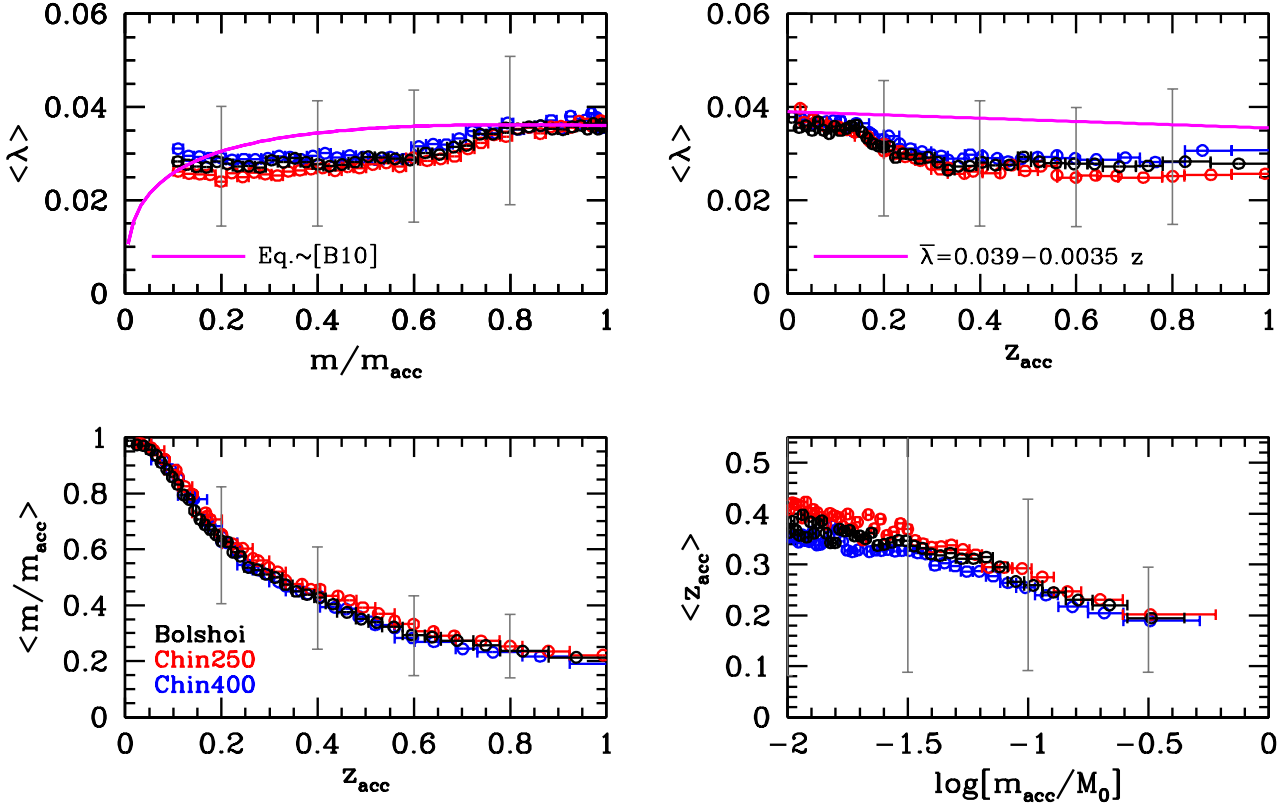


Figure 5. Correlations between subhalo properties. Clockwise from the upper left, the panels show the average spin parameter, λ , as function of m/m_{acc} and z_{acc} , the average mass ratio m/m_{acc} as function of z_{acc} , and the average accretion redshift, z_{acc} , as function of $\log[m_{\text{acc}}/M_0]$. As in Figs. 3 and 4, different colors correspond to different simulations, as indicated, horizontal errorbars indicate bin width, and vertical errorbars indicate the 16-84 percentiles. Note that (i) subhaloes that have lost a large fraction of their mass at accretion have lower spin, (ii) subhaloes that were accreted more recently have larger spin, (iii) subhaloes that are accreted later have lost a smaller fraction of their mass to tidal stripping, and (iv) subhaloes with a larger mass at accretion are accreted later. The thick, magenta line in the upper-left panel corresponds to a simple prediction based on outside-in stripping (see §4.2 and Appendix B), while the thick, magenta line in the upper-right panel indicates the redshift dependence of the average halo spin parameter of Hetzner & Burkert (2006).

4.1 Segregation of Virial Ratio

As shown in §3.2, the segregation of the virial ratio $T/|U|$ is strong with respect to r/r_{vir} , but almost absent with respect to the orbital energy, $E/|\Phi_0|$. This suggests that strong enhancements of $T/|U|$, reflecting strong deviations from virial equilibrium, are not a characteristic of certain orbits, but rather of certain orbital phases, and indicates that the radial segregation of $T/|U|$ is due to impulsive heating. During its peri-centric passage, the subhalo experiences a rapidly varying external potential (due to the host halo). According to the impulse approximation, this increases the kinetic energy of the constituent particles, causing a boost in $T/|U|$ that brings the subhalo out of virial equilibrium (see e.g., Mo, van den Bosch & White 2010). Subsequently, as the subhalo travels back out to apo-center, re-virialization drives $T/|U|$ of the subhalo back to 1/2. Hence, subhaloes predominantly have an enhanced value of $T/|U|$ close to peri-center, and not along their entire orbit (see also §4.4 below). This explains why $T/|U|$ is (strongly) segregated with respect to radius, but only weakly with respect to orbital energy. The weak segregation with respect to $E/|\Phi_0|$ arises because more bound orbits have smaller peri-centric distances, and there-

fore experience stronger tidal shocking, resulting in a larger average $T/|U|$ along their orbit.

As is evident from the lower panels of Fig. 4, the average $T/|U|$ is always well in excess of the virial value, 1/2, indicating that the average subhalo is never really in virial equilibrium. This is expected given that the internal dynamical time of a subhalo is basically the same as that of its host halo. Given that it takes at least a dynamical time to re-adjust virial equilibrium after an impulsive shock, and given that subhaloes typically experience one impulsive shock per orbit (during peri-centric passage), it should not come as a surprise that $\langle T/|U| \rangle > 0.5$. In addition, we emphasize that the surface pressure on subhaloes can also be substantial, which may also contribute to boosting the virial ratio above one half.

4.2 Segregation of Spin Parameter

As shown in Fig. 4, subhaloes with smaller spin parameters are segregated towards the center of their host halo, in good agreement with the findings of Reed et al. (2005) and Onions et al. (2013). Both Reed et al. and Onions et al. argue that high angular momentum material is more vulnerable to

stripping than low angular momentum, so that mass stripping will tend to lower the spin parameter. In this picture the segregation of spin parameter is merely an outcome of the segregation of m/m_{acc} .

This idea, that mass stripping lowers the spin parameter, is qualitatively consistent with the notion that angular momentum is less centrally concentrated within haloes than mass (e.g., Navarro & Steinmetz 1997; Bullock et al. 2001; Dutton & van den Bosch 2012), and is supported by the upper-left panel of Fig. 5, which shows that subhaloes that have lost a larger fraction of their mass have lower spin parameters. To test this idea in detail, we have computed the average spin parameter profile, $\lambda(< r)$, defined as the spin parameter of the material interior to radius r . We assume that halos follow a NFW density distribution with concentration parameter $c = 15$, and that their specific angular momentum at radius r follows $j(r) \propto [M(< r)]^{1.3}$, which is a good description of the average specific angular momentum profile of dark matter haloes (Bullock et al. 2001). $M(< r)$ is the mass enclosed within radius r . Next we use this spin parameter profile to predict the relation between λ and m/m_{acc} by assuming that the spin parameter of a subhalo is equal to its original spin (prior to mass stripping) inside the radius that encloses the mass m (see Appendix B for details). In other words, it is assumed that stripping proceeds in an outside-in fashion, much like peeling the layers of an onion, and that the angular momentum of the non-stripped material is unaffected. The solid, magenta line in the upper-left panel of Fig. 5 shows the resulting prediction for the relation between λ and m/m_{acc} , where we have normalized λ to fit the simulation data at $m/m_{\text{acc}} = 1$. This simple ‘onion model’ predicts that λ increase with m/m_{acc} , in qualitative agreement with the simulation results[¶]. However, in detail the prediction is clearly a poor description of the data.

Consequently, we do not think that this ‘onion’ model is the complete picture. In fact, there are good reasons to expect it to be incomplete. After all, whenever tidal forces on a subhalo are large enough to strip a significant fraction of its mass, clearly the tidal forces are also strong enough to torque the remaining core. Hence, the spin parameter of subhaloes is likely to be directly influenced, and modified, by the tidal field of its host. Indeed, several studies have shown that subhaloes tend to be radially aligned, in that their major axis points in the direction of the center of the host halo (e.g., Kuhlen et al. 2007; Pereira, Bryan & Gill 2008; Faltenbacher et al. 2008). This alignment is largely preserved as the subhalo undergoes its peri-centric passage, indicating that it indeed experiences a torque from the host. We leave it for a future study to investigate how exactly such torques modify the spin parameters of subhaloes. At this stage, we merely point out that is likely an important, additional mechanism for understanding the spin parameters of dark matter subhaloes, including their segregation.

Finally, we briefly mention another effect that might contribute to the segregation of subhalo spin. As shown by

[¶] This is opposite to the average spin profile derived for subhaloes by Onions et al. (2013); However, as we show in Appendix B, the Onions et al. results are an artefact of poorly resolved haloes.

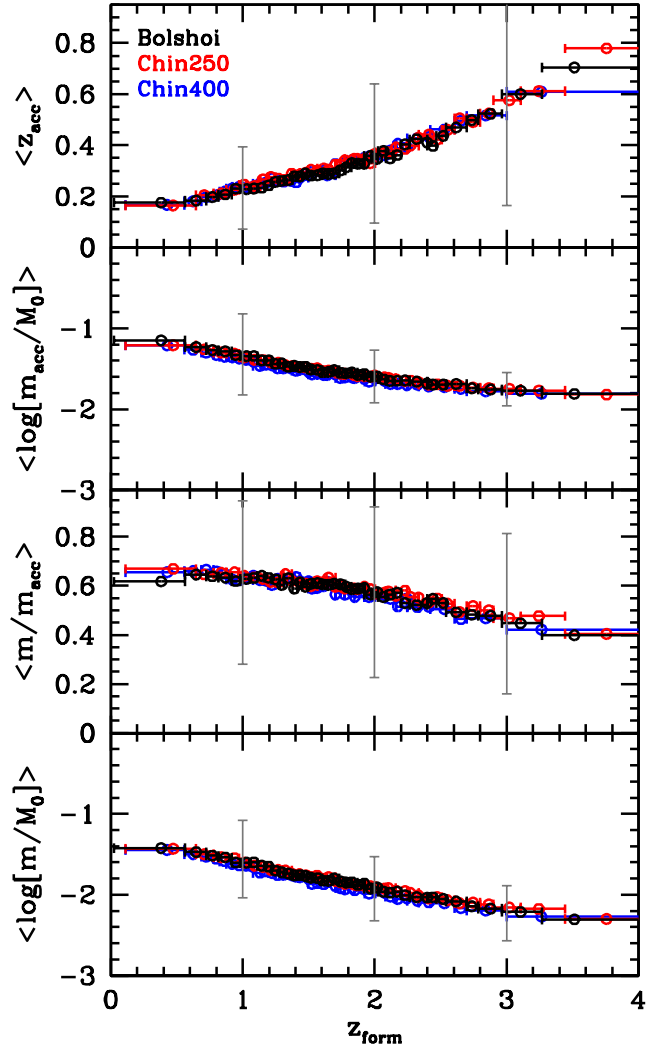


Figure 6. Correlations between various subhalo properties and the subhalo’s formation redshift. From top to bottom, the subhalo properties plotted are the accretion redshift, the mass at accretion, the mass ratio m/m_{acc} , and the present-day subhalo mass. The various trends are discussed in detail in §4.3. Color coding and horizontal errorbars are as in the previous figures.

Hetznecker & Burkert (2006), the average spin parameter of dark matter haloes evolves with redshift as

$$\bar{\lambda}(z) \simeq 0.039 - 0.0035 z. \quad (9)$$

If we postulate that this redshift evolution is arrested when a halo becomes a subhalo, then subhaloes that were accreted earlier would have a smaller spin parameter on average (at least at infall). Since haloes that accreted earlier are segregated towards the center, this could potentially explain the observed segregation of subhalo spin parameter. The upper-right panel of Fig. 5 shows that indeed subhaloes with a lower spin parameter were accreted at higher redshifts. However, the trend is inconsistent with the expectations from Eq. (9), indicated by the thick, magenta line. The redshift evolution of $\bar{\lambda}$ is simply too weak to have an impact on the subhaloes, the majority of which were accreted relatively recently ($z_{\text{acc}} < 0.5$). It is interesting, though, that most of the correlation between λ and z_{acc} seems confined to the range

$0.1 \lesssim z_{\text{acc}} \lesssim 0.3$. As we will see below, subhaloes accreted in this interval are between their first peri- and first apo-centric passages, and the data seems to suggest that this period is critical for regulating the subhalo spin parameter.

4.3 Segregation of Formation Redshift

As we have shown, subhaloes are weakly segregated in their formation redshift, with those that form earlier located closer to the center of their host halo. As we demonstrate below, the origin of this segregation is indirect, and arises from the fact that the formation redshift of subhaloes is correlated with a number of other subhalo properties, each of which is segregated. Fig. 6 shows how subhaloes with a higher formation redshift (i) are accreted earlier, (ii) are less massive at accretion, (iii) have lost more mass since accretion, and (iv) have a smaller present-day mass. Results (i) and (ii) are manifestations of hierarchical structure formation. Result (iii) is a natural outcome of (i), when one takes into account that subhaloes that were accreted earlier have been exposed to mass stripping for a longer period of time (see §4.5). And finally, result (iv) is a consequence of (ii) and (iii) combined. Note that the correlation between z_{form} and z_{acc} has previously been pointed out in Hearin et al. (2014).

In terms of segregation, result (i) would imply that subhaloes that form earlier are segregated towards the center of their host halo. After all, subhaloes with larger z_{acc} are on more bound orbits. This is qualitatively consistent with the fact that the r_s values for z_{form} are negative. However, this is counter-balanced by result (ii), and the fact that subhaloes that are less massive at accretion are segregated towards the outskirts of their host halo. These two competing effects result in a final segregation for z_{form} that is weak. It also explains why the correlation between z_{form} and $E/|\Phi_0|$ is non-monotonic (cf. Fig. 4).

4.4 Segregation of Accretion Redshift

Subhaloes are strongly segregated in their accretion redshift, with early-accreted subhaloes residing on more bound orbits. This has its origin in the inside-out assembly of dark matter haloes. Fig. 7 plots the average, normalized radius, $\langle r/r_{\text{vir}} \rangle$, the average virial ratio, $\langle T/|U| \rangle$, and the average orbital energy, $\langle E/|\Phi_0| \rangle$, as functions of z_{acc} . Note how the average halo-centric distance, which is averaged over tens of thousands of subhaloes, clearly reveals the characteristics of an orbit, at least for $z_{\text{acc}} \lesssim 0.5$. Subhaloes accreted at $z_{\text{acc}} \sim 0.1$ have just reached their first peri-center, while subhaloes that are at their first apo-centric passage after accretion typically where accreted around $z_{\text{acc}} \sim 0.25$. Note how the middle panel shows that the average $T/|U|$ of subhaloes experiences a temporary boost shortly after first pericentric passage, in accordance with the impulsive heating picture sketched above in §4.1.

As the lower panel shows, subhaloes accreted earlier are more bound. This could have two explanations. Either this could simply reflect that at earlier times the main progenitor of the host was smaller, so that accretion ‘naturally’ occurred at smaller halo-centric distances, or it could be that subhaloes that were accreted earlier were exposed to dynamical friction for a longer period, resulting in a more negative

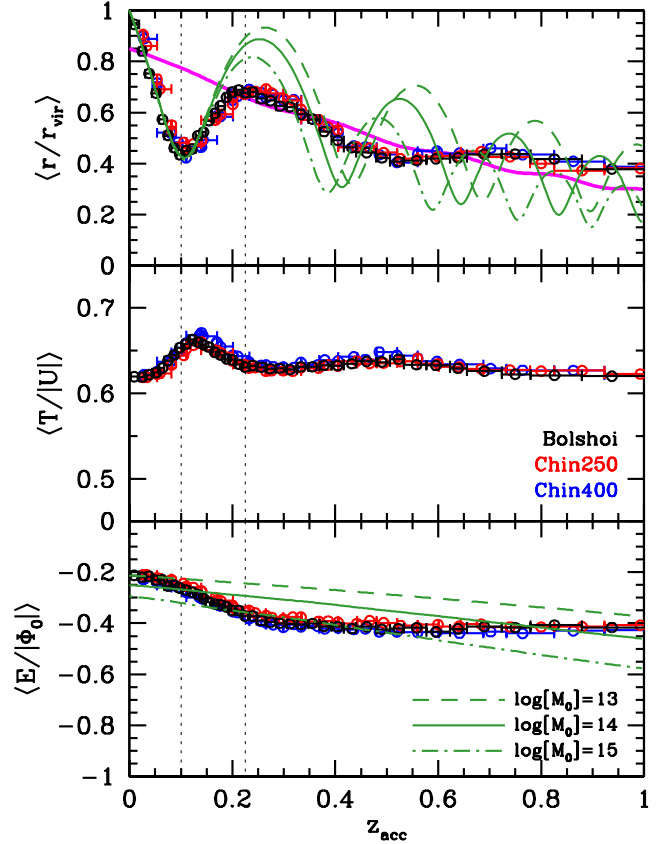


Figure 7. As a function of subhalo accretion redshift, the various panels show, from top to bottom, the average halo-centric radius, r/r_{vir} , the average virial ratio $T/|U|$, and the average orbital energy, $E/|\Phi_0|$. The green lines are predictions from the ‘adiabatic evolution model’ described in the text, for three different host halo masses, M_0 , as indicated in the lower panel. The thick, magenta curve is the prediction from the same model, but for subhaloes which at accretion start out on a circular orbit. The vertical dotted lines indicate the accretion redshifts of subhaloes that are currently (at $z = 0$) experiencing their first peri- and apo-centric passage. Color coding and horizontal errorbars are as in the previous figures.

binding energy today. We now proceed to demonstrate that the former dominates.

Let $M(z)$, $r_{\text{vir}}(z)$ and $c(z)$ be the virial mass, virial radius and concentration of the main progenitor of a host halo of present-day mass M_0 . If we assume that this main progenitor can, at any redshift, be described by an NFW profile, then the corresponding time-varying gravitational potential is

$$\Phi(r, z) = -\frac{GM(z)}{r_{\text{vir}}(z)} \frac{\ln[1 + xc(z)]}{xf[c(z)]}, \quad (10)$$

where $x = r/r_{\text{vir}}(z)$ and $f(x)$ is given by Eq. (3). If we assume that the time-variability of $\Phi(r, z)$ is sufficiently slow, so that the system responds adiabatically, then, given an initial (at accretion) orbital energy, E_{orb} , and angular momentum, L_{orb} , and ignoring dynamical friction, we can predict the current (i.e., at $z = 0$) location and orbital energy of a subhalo accreted at z_{acc} , by simple integration of its orbit in the time-varying potential $\Phi(r, z)$. We refer to this as our ‘adiabatic evolution model’. In order to specify the initial

orbit at accretion, we introduce the orbital parameters α and η , defined by

$$E_{\text{orb}} = E_{\text{circ}}(\alpha r_{\text{acc}}), \quad L_{\text{orb}} = \eta L_{\text{circ}}(\alpha r_{\text{acc}}). \quad (11)$$

Here $r_{\text{acc}} \equiv r_{\text{vir}}(z_{\text{acc}})$ is the virial radius of the main progenitor at the accretion redshift, and $E_{\text{circ}}(r)$ and $L_{\text{circ}}(r)$ are the orbital energy and angular momentum of a circular orbit of radius r . Thus defined, $\eta = 0$ and 1 correspond to purely radial and circular orbits, respectively, while $\alpha = 1$ corresponds to the orbital energy of a circular orbit with radius $r = r_{\text{acc}}$.

We now proceed as follows. For a given M_0 , we use the publicly available^{||} code of van den Bosch et al. (2014) to compute the *average* mass accretion history $\langle M(z)/M_0 \rangle$ adopting the same cosmology as for the Bolshoi simulation. The same code also provides the redshift evolution of the halo concentration parameter, $c(z)$, and therefore allows a straightforward computation of the time-varying potential $\Phi(r, z)$ of the *average* main progenitor of M_0 . Given a z_{acc} , and assuming values for α and η , we then integrate the subhalo's orbit to $z = 0$ in the time-dependent host potential, $\Phi(r, z)$, using a fifth-order Cash-Karp Runge-Kutta method (Cash & Karp 1990) with adaptive step-size control (e.g., Press et al. 1992). Using the resulting location and velocity of the subhalo at $z = 0$, we then compute the corresponding r/r_{vir} and $E/|\Phi_0|$, where r_{vir} and Φ_0 are the virial radius and central potential of the host halo at the present time.

The results, for three different values of M_0 , as indicated, are shown as green curves in the upper and lower panels of Fig. 7. Here we have tuned α and η to match the peri-centric passage around $z \sim 0.1$, which results in $(\alpha, \eta) = (0.85, 0.83)$. Note how the phases of orbits for the three different host halo masses remain nicely in sink until roughly the first apo-centric passage, after which the orbital phases rapidly decohere. This is entirely due to the fact that different host halo masses have different mass accretion histories, and nicely explains why the average r/r_{vir} of subhaloes no longer reveals pronounced apo- and peri-centric passages for $z_{\text{acc}} \gtrsim 0.5$. Note also how there is a clear increase of the (orbit-averaged) r/r_{vir} with decreasing z_{acc} , reflecting the inside-out growth of the host halo. To illustrate this trend without the radial excursions due to non-circularity of the orbits, the thick, magenta curve in the upper panel of Fig. 7 corresponds to the z_{acc} dependence of r/r_{vir} in the case of $M_0 = 10^{14} h^{-1} M_{\odot}$ for orbits that at accretion have $(\alpha, \eta) = (0.85, 1.0)$, corresponding to a circular orbit at $r = 0.85 r_{\text{acc}}$. Clearly, this provides a good description of the average trend, and therewith demonstrates that the segregation of z_{acc} is mainly a manifestation of the slow, inside-out growth of the host haloes. This is also supported by the lower-panel of Fig. 7, which shows that the overall trend of $E/|\Phi_0|$ with z_{acc} is in line with the predictions from the orbit integrations.

Although our adiabatic evolution model nicely reproduces the main trends, there are also a few noteworthy differences. First of all, the model, which is tuned to reproduce the first peri-centric passage, dramatically overpredicts the r/r_{vir} at around the first apo-centric crossing after infall.

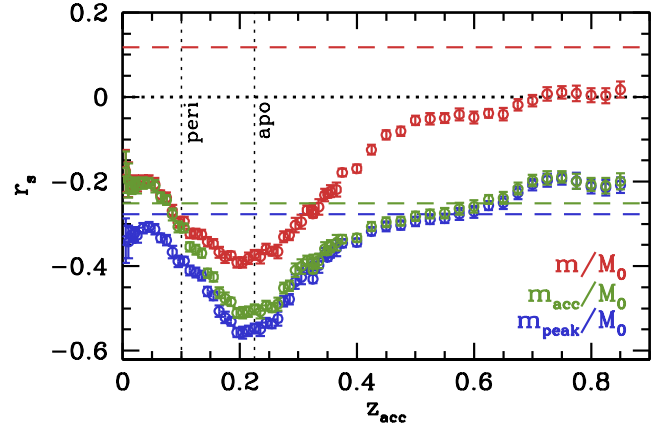


Figure 8. The Spearman rank-order correlation coefficient between the orbital energy, $E/|\Phi_0|$, and m/M_0 (red symbols), m_{acc}/M_0 (green symbols) and m_{peak}/M_0 (blue symbols), as a function of z_{acc} . The horizontal dashed lines of the same color indicate the corresponding values of r_s for the entire sample of subhaloes (not split by accretion time). The black, horizontal dotted curve corresponds to no-segregation ($r_s = 0$), and is plotted to guide the eye. In making this plot we have used a sliding bin, with a width of 0.05 for $z_{\text{acc}} < 0.4$ and 0.15 for $z_{\text{acc}} > 0.4$. The larger bin width for larger z_{acc} is required to assure sufficient numbers of subhaloes per bin. Note how subhaloes are already segregated *at accretion*, how this is dramatically magnified during the first radial orbit due to dynamical friction, after which mass stripping, tidal disruption and the demise of efficient dynamical friction cause the segregation strength to decrease again.

This is an artifact of the fact that subhaloes in the simulation boxes have to be located within the virial radius of their host. Our model predicts that the *average* subhalo that was accreted around $z_{\text{acc}} \sim 0.25$ is located close to the virial radius r_{vir} of the present-day host halo. This means that close to 50 percent of the subhaloes will have an apo-center that lies outside of r_{vir} , and those subhaloes will therefore not be included in our sample (most of them will instead be identified as host haloes by the ROCKSTAR halo finder). Such subhaloes, that have moved out beyond the virial radius are often called ‘backsplash’ or ‘ejected’ haloes, and have been the topic of a number of recent studies (e.g., Balogh et al. 2000; Mamon et al. 2004; Gill, Knebe & Gibson 2005; Sales et al. 2007; Ludlow et al. 2009; Teyssier, Johnston & Kuhlen 2012; Wetzel et al. 2014). As a consequence, the *average* r/r_{vir} of the subhaloes in our sample will be lower than predicted by the adiabatic evolution model, especially for subhaloes whose accretion redshift has them experience their first apo-centric passage around $z = 0$. This also explains largely why, over the range $0.15 \lesssim z_{\text{acc}} \lesssim 0.4$, the simulation results reveal a more negative $E/|\Phi_0|$ than predicted by our model. In addition to this artifact that arises from backplash haloes, it is important to realize that individual host haloes do not evolve adiabatically, but may grow by major mergers during which they experience violent relaxation, and that massive subhaloes (those with an instantaneous mass ratio $m/M \gtrsim 0.1$) experience dynamical friction that causes an evolution in the orbital energy and angular momentum that is not accounted for in our orbit integration (but see §4.6). Despite these shortcomings, it is clear that the simple adiabatic evolution model captures most of the

^{||} <http://www.astro.yale.edu/vdbosch/PWGH.html>

main trends, supporting the notion that the segregation of z_{acc} can largely be understood as arising from the inside-out growth of the host haloes.

4.5 Segregation of Retaining Mass Fraction

Similar to accretion redshift, the fraction of the accretion mass that is retained in the present-day subhalo is extremely strongly segregated, with subhaloes that have lost a larger fraction of their accretion mass residing on more bound orbits. The key to understanding the origin of this strong segregation of m/m_{acc} is provided by the lower-left panel of Fig. 5, which plots the average m/m_{acc} as function of z_{acc} . Clearly, subhaloes that were accreted earlier have lost a larger fraction of their infall mass, which is simply a consequence of the fact that they have been exposed to tidal stripping for a longer period (cf. Gao et al. 2004; van den Bosch, Tormen & Giocoli 2005; Zentner et al. 2005; Giocoli et al. 2010; Jiang & van den Bosch 2014). Combining this with the strong segregation of z_{acc} , discussed in §4.4, immediately explains, both qualitatively and quantitatively, why m/m_{acc} is so strongly segregated as well. Note that subhaloes that were accreted around $z_{\text{acc}} = 0.3$ have on average lost half of their mass at accretion.

4.6 Segregation of Accretion Mass and Peak Mass

The segregation by accretion mass, m_{acc}/M_0 , with subhaloes with larger m_{acc}/M_0 residing close to the center of their host halo, has its origin in a combination of three effects. First of all, the lower-right panel of Fig. 5 shows that subhaloes with a larger accretion mass were accreted more recently, which is simply a manifestation of hierarchical structure formation. If this were the only effect, then based on the strong segregation of z_{acc} , subhaloes with a larger accretion mass should be on *less* bound orbits. This is opposite to the trend seen in the simulation data, indicating that other, more important effects must be playing a role.

To get some insight, we can take out the z_{acc} effect by examining the segregation of m_{acc}/M_0 for different (narrow) bins in accretion redshift. This is done in Fig. 8, where the green symbols show the Spearman rank-order correlation coefficient between m_{acc}/M_0 and $E/|\Phi_0|$ as function of z_{acc} . Each data point corresponds to a narrow bin in z_{acc} , as described in the figure caption. The green, dashed horizontal line indicates the corresponding r_s value for the entire sample. Note first of all, that even at $z_{\text{acc}} = 0$ there is a non-zero correlation between m_{acc}/M_0 and orbital energy, in the sense that more massive subhaloes are on more bound orbits. Hence, part of the segregation of m_{acc}/M_0 is already imprinted in the infall conditions!

We emphasize, though, that this initial (i.e. meaning ‘at accretion’) correlation is fairly weak; this is shown explicitly in the upper panel of Fig. 9, which shows the average orbital energy, $\langle E/|\Phi_0| \rangle$ as function of m_{acc}/M_0 for subhaloes with $z_{\text{acc}} < 0.05$ (i.e., shortly after their accretion). Note how the most massive subhaloes at infall are on slightly more bound orbits, but that the dependence vanishes for $m_{\text{acc}} \lesssim M_0/10$, in qualitative agreement with the results of Wetzel (2011; cf. their Fig. 6) and Jiang et al. 2015.

Between $z_{\text{acc}} = 0$ and $z_{\text{acc}} \sim 0.25$ there is a dramatic in-

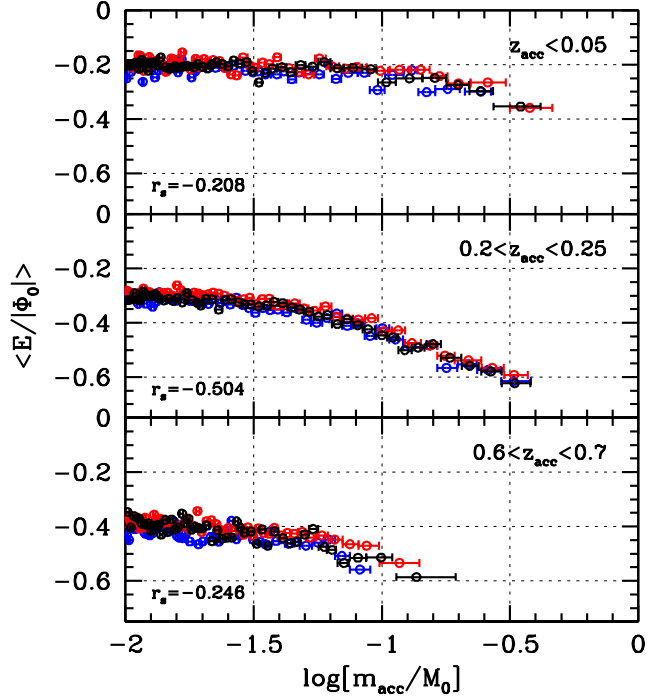


Figure 9. The average orbital energy as function of the mass at accretion for subhaloes in three different bins of accretion redshift. The upper panel corresponds to $z_{\text{acc}} < 0.05$, and shows that subhaloes already reveal a weak dependence of orbital energy on m_{acc}/M_0 at accretion. The middle panel corresponds to $0.2 < z_{\text{acc}} < 0.25$, which is the range of accretion redshifts for which the Spearman rank-order correlation coefficient is most negative (cf. Fig. 8), and roughly coincides with subhaloes that, at the present day, have reached their first apo-centric passage. Finally, the lower panel corresponds to $0.6 < z_{\text{acc}} < 0.7$, for which subhaloes have once again a r_s that is comparable to that at infall.

crease in the segregation strength of m_{acc}/M_0 , with r_s dropping from -0.2 for $z_{\text{acc}} = 0$ to -0.5 at $z_{\text{acc}} = 0.25$. The middle panel of Fig. 9 plots $\langle E/|\Phi_0| \rangle$ as function of m_{acc}/M_0 for subhaloes with $0.2 < z_{\text{acc}} < 0.25$, clearly revealing a very strong correlation between accretion mass and orbital energy. As we demonstrate below, this is due to dynamical friction operating on the most massive subhaloes. For $z_{\text{acc}} > 0.25$ the Spearman rank-order correlation coefficient becomes less negative again, slowly asymptoting to roughly the sample-averaged value of $r_s = -0.251$ for $z_{\text{acc}} \gtrsim 0.6$. This is due to the fact that subhaloes that experience the strongest dynamical friction also experience most mass loss: after all, dynamical friction results in smaller peri-centric distances, and thus stronger tidal forces. At large z_{acc} , this means that the subhaloes that were most segregated are also more likely to have $m/m_{\text{acc}} < 0.1$ or to be tidally disrupted, and therefore to be absent from our sample. This will diminish the segregation strength of m_{acc}/M_0 . An additional effect is that, as we will demonstrate below, dynamical friction is no longer efficient for subhaloes with $z_{\text{acc}} \gtrsim 0.25$. This can be understood from the fact that dynamical friction is only efficient for subhaloes with a mass that is larger than roughly ten percent of the host mass. For smaller mass ratios, the dynamical friction time scale exceeds the Hubble time (e.g., Binney & Tremaine 2008; Mo et al. 2010). As is evident from the upper-left panel of Fig. 5, subhaloes

with $z_{\text{acc}} \gtrsim 0.25$ have *on average* lost more than 50 percent of their accretion mass, and this will be even larger for subhaloes that experienced significant dynamical friction. Consequently, in almost all cases subhaloes with $z_{\text{acc}} \gtrsim 0.25$ have already lost so much mass that dynamical friction is no longer important. The correlation between $\langle E/|\Phi_0| \rangle$ and m_{acc}/M_0 for subhaloes with $0.6 < z_{\text{acc}} < 0.7$ is shown in the lower panel of Fig. 9, and is comparable to that at infall (i.e., for $z_{\text{acc}} < 0.05$ shown in the upper panel), modulo a shift that mainly reflects the evolution of the host halo.

To better illustrate the impact of dynamical friction, Fig. 10 shows once again the average r/r_{vir} and $E/|\Phi_0|$ of subhaloes as function of z_{acc} , but this time we have split the sample of subhaloes in three bins of $\log[m_{\text{acc}}/M_0]$, as indicated. For comparison, the green-shaded bands show the predictions from our adiabatic evolution model discussed in §4.4. Subhaloes with $m_{\text{acc}}/M_0 < 0.1$ closely follow the predictions from the adiabatic evolution model^{***} indicating that they do not experience significant dynamical friction. However, subhaloes with a larger infall mass reach a smaller peri-centric distance at $z_{\text{acc}} \sim 0.1$, and a much smaller apo-centric distance at $z_{\text{acc}} \sim 0.25$. This is the outcome of dynamical friction operating during the first radial orbit. This is even more evident from the lower panel, which shows that the massive subhaloes experience a much stronger increase in binding energy than subhaloes with a smaller infall mass, but only for $z_{\text{acc}} \lesssim 0.25$, which roughly coincides with first apo-centric passage.

The entire discussion above regarding the accretion mass also applies to the peak mass. The only difference is that the initial segregation *at infall* is significantly larger for m_{peak}/M_0 ($r_s \simeq -0.33$) than for m_{acc}/M_0 ($r_s = -0.21$). Other than that, the results for m_{peak}/M_0 look indistinguishable from those for m_{acc}/M_0 for $z_{\text{acc}} \gtrsim 0.2$ (see blue symbols in Fig. 8).

To summarize, part of the segregation of m_{acc}/M_0 and m_{peak}/M_0 is already imprinted in the infall conditions. It is further boosted by dynamical friction operating on the most massive subhaloes, but only during their first radial orbit. Tidal disruption subsequently diminishes the segregation of m_{acc}/M_0 , as does the fact that subhaloes with larger accretion masses are accreted later.

4.7 Segregation of Present-day Subhalo Mass

As already mentioned in §3.1 the segregation of present-day subhalo mass is weak and strongly dependent on sample selection. It has its origin in a combination of many of the effects discussed above. Some insight can be gained from Fig. 8, where the red symbols show the Spearman rank-order correlation coefficient between m/M_0 and $E/|\Phi_0|$ for narrow bins in z_{acc} . Overall the trend with accretion redshift is very similar to that for m_{acc}/M_0 , except that r_s doesn't become as negative and asymptotes to zero for large z_{acc} . This is because the segregation of m is influenced by both dynamical friction and mass stripping, with the latter diminishing the impact of the former.

^{***} As discussed in §4.4, the mismatch between model and simulation results around the first apo-centric passage ($z_{\text{acc}} \sim 0.25$) is an artifact related to ejected subhaloes.

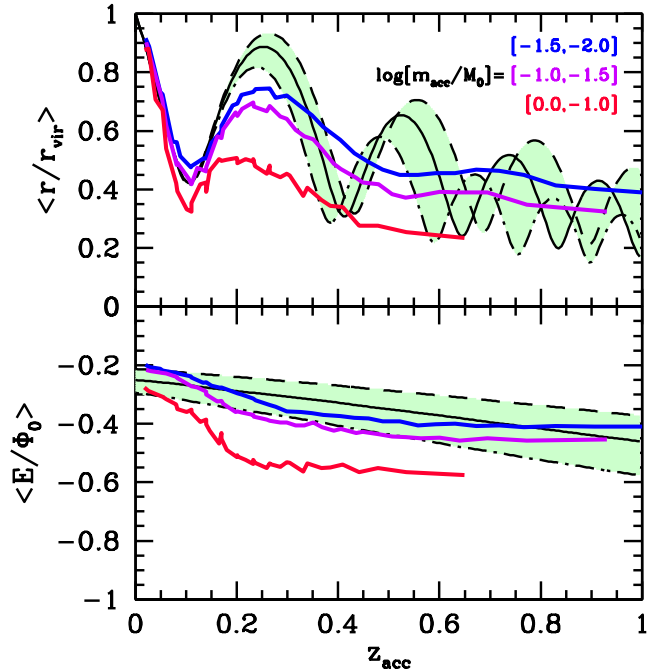


Figure 10. Similar to Fig. 7 (but with middle panel absent). The green shaded region marks the predictions from the adiabatic evolution model discussed in §4.4. The thick, colored lines are the average halo-centric radii (upper panel) and orbital energies (lower panel) for subhaloes in three bins of m_{acc}/M_0 , as indicated. Here we have combined the results from the three different simulation boxes, in order to boost statistical power. Even then the results remain somewhat noisy, as is evident from the jaggedness of the lines. Note how subhaloes with $m_{\text{acc}}/M_0 > 0.1$ reside on orbits with smaller peri- and apo-centric distances, as a consequence of dynamical friction operating during the first radial orbit. The latter is evident from the lower panel, which shows that subhaloes with $m_{\text{acc}}/M_0 > 0.1$ experience a change in orbital energy that is much larger than predicted by the adiabatic evolution model.

Note that for all z_{acc} bins shown, r_s is well below the value for the entire sample ($r_s = +0.118$), indicated by the red horizontal dashed line. Although this may seem counterintuitive at first, it simply arises from the fact that the segregation of present-day subhalo mass is dominated by a strong correlation between m/M_0 and z_{acc} , in the sense that subhaloes with a larger present-day mass have been accreted more recently, and are therefore on less bound orbits. This strong correlation between m/M_0 and z_{acc} is partially a consequence of our sample selection. By only selecting subhaloes with $m_{\text{acc}}/M_0 \geq 0.01$, subhaloes with $\log[m/M_0] = -3$ must have $m/m_{\text{acc}} = 0.1$, and therefore have been accreted a long time ago (cf. upper-left panel of Fig. 5). If we modify the sample selection, and also allow for subhaloes with $-3 \leq \log[m_{\text{acc}}/M_0] < -2$ (which includes the subhaloes located in the pink-shaded triangular region labeled ‘A’ in Fig. 1), the correlation between m/M_0 and z_{acc} is *much* weaker (at least for $m/M_0 < -2$). Less of the impact of dynamical friction is now ‘washed away’, resulting in a (slightly) negative value for r_s . See Appendix A for a more detailed discussion of the impact of sample selection on the mass segregation of subhaloes.

5 SUMMARY & DISCUSSION

We have presented a comprehensive analysis of the segregation of dark matter subhaloes in their host haloes. Using three different simulations, run with two different N -body codes, we examined the segregation of 12 different subhalo properties with respect to three different segregation indicators: halo-centric distance, r/r_{vir} , (specific) orbital energy, $E/|\Phi_0|$, and the projected halo-centric distance, R/R_{vir} . We find all twelve properties to be significantly segregated with respect to all three indicators, except for one: $V_{\text{max}}/V_{\text{vir},0}$, the present-day maximum circular velocity of subhaloes, normalized by the virial velocity of the host halo, is the only subhalo property that is consistent with having no significant correlation with orbital binding energy. In general, subhalo properties are most strongly segregated with respect to orbital energy. The segregation with respect to r/r_{vir} is typically weaker, as expected from the fact that the typical orbits of subhaloes have apo-to-pericenter ratios of 6 : 1 (e.g., Ghigna et al. 1998; van den Bosch et al. 1999), which washes out the segregation strength. As expected, the segregation is weakest with respect to R/R_{vir} , with a Spearman rank-order correlation coefficient that is, due to projection, typically $\sim 20\%$ smaller (in absolute terms) than that for r/r_{vir} .

One of the most strongly segregated subhalo properties is the subhalo accretion redshift, z_{acc} . Subhaloes that were accreted earlier are segregated more towards the center of their host, and are on more bound orbits. On average, the most bound quartile was accreted ~ 2.5 to 3.0 Gyr earlier than the least bound quartile. As we have demonstrated by integrating typical subhalo orbits in the time-evolving potential of the host halo, computed using the average mass assembly histories of van den Bosch et al. (2014), the strong segregation of z_{acc} is an outcome of the inside out assembly of their host haloes. Subhaloes that were accreted around $z_{\text{acc}} = 0.1$ are presently experiencing their first pericentric passage of the host, while subhaloes at their first apo-centric passage were typically accreted around $z_{\text{acc}} = 0.25$. During their first radial orbit, subhaloes in different host haloes show strong phase-coherence. This diminishes with increasing z_{acc} as a consequence of the different mass assembly histories of their host haloes. During pericentric passage, subhaloes experience a tidal shock, which (temporarily) boosts their virial ratio, $T/|U|$. As a consequence, $T/|U|$ is strongly segregated with respect to halo-centric radius. However, since subhaloes re-establish virial equilibrium after their pericentric passage, there is only little segregation of $T/|U|$ with respect to the orbital energy. The latter arises from the fact that subhaloes on more bound orbits typically have smaller peri-centers, and therefore experience stronger tidal shocks.

The most strongly segregated subhalo properties are the mass ratio m/m_{acc} and the corresponding $V_{\text{max}}/V_{\text{acc}}$, which both decrease with increasing binding energy of the orbit. This has its origin in the strong segregation of z_{acc} combined with a strong correlation between m/m_{acc} (and also $V_{\text{max}}/V_{\text{acc}}$) and z_{acc} (cf. upper-left panel of Fig. 5). The latter is simply a manifestation of the fact that the (orbit-averaged) mass of a subhalo is well represented by $m(t) = m_{\text{acc}} \exp[-(t - t_{\text{acc}})/\tau_{\text{dyn}}]$, with τ_{dyn} the (instantaneous) dynamical time of the host halo (van den Bosch et

al. 2005; Giocoli et al. 2008, 2010). Hence, the mass ratio m/m_{acc} is predominantly set by the time since accretion. Subhaloes that were accreted around $z_{\text{acc}} = 0.3$ have on average lost half of their mass at accretion.

The mass of a subhalo at accretion, m_{acc} , is fairly strongly segregated, in that subhaloes that are more massive at accretion are found on more bound orbits, and at smaller halo-centric distances. As we have shown, the segregation of m_{acc}/M_0 is already imprinted (at least partially) in the infall conditions. It is further boosted by dynamical friction operating on the most massive subhaloes, but only during their first radial orbit. The tidal disruption of subhaloes in the numerical simulations subsequently diminishes the segregation of m_{acc}/M_0 , as does the fact that subhaloes with larger accretion masses are accreted later. The peak subhalo mass, m_{peak} , reveals similar segregation properties as m_{acc} . The dependence of m_{peak} on orbital energy at infall is even stronger than for the accretion mass, which explains why the overall segregation strength of m_{peak}/M_0 is slightly larger than for m_{acc}/M_0 . Finally, we emphasize that the maximum circular velocities V_{acc} and V_{peak} have segregation properties that are similar to, but slightly stronger than, their corresponding masses.

The strong segregation of m_{acc} and V_{acc} has important ramifications. In the framework of subhalo abundance matching (hereafter SHAM), it is assumed that the luminosities and/or stellar masses of galaxies are tightly correlated with m_{acc} or V_{acc} (e.g., Vale & Ostriker 2004, 2006; Kravtsov et al. 2004, 2014; Conroy, Wechsler & Kravtsov 2006; Conroy & Wechsler 2009; Behroozi, Conroy & Wechsler 2010; Guo et al. 2010; Trujillo-Gomez et al. 2011; Rodríguez-Puebla, Drory & Avila-Reese 2012). If this is indeed the case, as suggested by the success of SHAM in reproducing galaxy clustering, then galaxy stellar masses and/or luminosities must be significantly segregated. Recently, Reddick et al. (2013) argued that abundance matching works the best (i.e., best matches the observed clustering) if stellar masses are matched to the peak circular velocity of their halo, V_{peak} . As is evident from Table 3, the segregation strength for V_{peak} is even stronger than for m_{acc} or V_{acc} , which would thus imply even stronger segregation by luminosity or stellar mass. Put differently, one can use the observed strength of luminosity and/or stellar mass segregation, combined with the results presented here, to put tight constraints on the galaxy-dark matter connection. We will explore this avenue in future work.

The present-day mass of subhaloes, and in particular the corresponding present-day maximum circular velocity, V_{max} , show surprisingly little segregation. In particular, the relation between m/M_0 and $E/|\Phi_0|$ is non-monotonic, while $V_{\text{max}}/V_{\text{vir},0}$ is the only subhalo property tested here that reveals no significant segregation with respect to orbital energy. This is a somewhat fortuitous outcome of a competition between various effects. The strong segregation evident in accretion (or peak) mass is no longer evident in the present-day halo mass because of mass stripping. Subhaloes that were accreted earlier, and that experienced stronger dynamical friction, have lost a larger fraction of their mass at accretion, which washes out the segregation imprinted due to both dynamical friction and the inside out assembly of the host halo.

In agreement with previous studies (Reed et al. 2005;

Onions et al. 2013), we find that subhaloes with smaller spin parameters are segregated towards the center of their host halo. Both Reed et al. and Onions et al. have argued that this is a natural consequence of mass stripping; subhaloes on more bound orbits have lost a larger fraction of their mass, and since angular momentum is less centrally concentrated within haloes than matter (Navarro & Steinmetz 1997; Bullock et al. 2001; Dutton & van den Bosch 2012), stripping will lower the spin parameter. However, we have shown that the radial dependence of the spin parameter profile $\lambda(< r)$ is too weak to explain the segregation of subhalo spin. We argue instead that the same tidal forces that strip subhaloes also exert torques that influence their spins.

Finally, we have shown that subhaloes are also segregated by their formation redshift, z_{form} , defined as the redshift at which the subhalo's main progenitor first reached a mass equal to half its peak mass. Typically, subhaloes that formed earlier have somewhat smaller halo-centric distances, but the correlation between z_{form} and $E/|\Phi_0|$ is not monotonic. The reason is that the segregation by z_{form} is indirect, and arises from correlations with two other subhalo properties that have both strong segregation, but in opposite directions: subhaloes that form earlier are, on average, also accreted earlier, and have smaller accretion masses. The weak radial segregation of z_{form} explains why Watson et al. (2015), when linking galaxy SFR to halo formation time using the age-matching technique (Hearin & Watson 2013), predict that the distribution of halo-centric distances of quenched satellites is shifted to smaller values compared to that of actively star forming satellites. This is in excellent agreement with observations, and thus seems to suggest a strong correlation between the SFRs of satellite galaxies and the formation time of their corresponding subhaloes. Although this supports a view in which the segregation by SFR in groups and clusters has its origin in the dark sector, we emphasize that it does not exclude the possibility that it instead arises from the environmental impact on galaxy evolution (cf. discussion in §1). As we have shown, subhaloes that form earlier are also accreted earlier (on average), and they have thus been exposed longer to satellite specific quenching mechanisms such as ram-pressure stripping, tidal stripping, and strangulation. In addition, quenched galaxies are typically more massive than active galaxies. If stellar mass is closely related to m_{acc} or m_{peak} , as suggested by SHAM, then the observed segregation of SFR might also be an indirect consequence of the segregation of m_{acc}/M_0 (or m_{peak}/M_0). In a forthcoming paper (Lu et al., in prep) we will place tighter constraints on the relation between the properties of satellite galaxies and their associated subhaloes using detailed observations of segregation in groups and clusters.

ACKNOWLEDGMENTS

We are indebted to Matt Becker for making the halo catalogs of his Chinchilla simulations available to us, and to Andrew Hearin and the anonymous referee for insightful comments, ideas and suggestions. This material is supported (in part) by the National Science Foundation under Grant No. PHY-1066293 and the hospitality of the Aspen Center for Physics. Support for PB was provided by a Giacconi Fellowship and an HST Theory grant; program number HSTAR-12159.01-

A was provided by NASA through a grant from the Space Telescope Science Institute, which is operated by the Association of Universities for Research in Astronomy, Incorporated, under NASA contract NAS5-26555.

REFERENCES

- Adami C., Biviano A., Mazure A., 1998, *A&A*, 331, 439
 Angulo R.E., Lacey C.G., Baugh C.M., Frenk C.S., 2009, *MNRAS*, 399, 983
 Balogh M. L., Navarro J. F., Morris S. L., 2000, *ApJ*, 540, 113
 Balogh M. L. et al., 2004, *MNRAS*, 348, 1355
 Balogh M. L. et al., 2014, *MNRAS*, 443, 2679
 Behroozi P.S., Conroy C., Wechsler R.H., 2010, *ApJ*, 717, 379
 Behroozi P.S., Wechsler R.H., Wu H.-Y., 2013a, *ApJ*, 762, 31
 Behroozi P. S., Wechsler R. H., Wu H.-Y., Busha M.T., Klypin A.A., Primack J.R., 2013b, *ApJ*, 763, 18
 Bett P., Eke V., Frenk C.S., Jenkins A., Helly J., Navarro J., 2007, *MNRAS*, 376, 215
 Binney J., Tremaine S., 2008, *Galactic Dynamics*, Princeton University Press
 Biviano A. et al., 1996, *A&A*, 311, 95
 Biviano A., Katgert P., Thomas T., Adami C., 2002, *A&A*, 387, 8
 Blanton M. R., Berlind A. A., 2007, *ApJ*, 664, 791
 Bryan G., Norman M., 1998, *ApJ*, 495, 80
 Bullock J.S., Dekel A., Kolatt T.S., Kravtsov A.V., Klypin A.A., Porciani C., Primack J.R., 2001, *ApJ*, 555, 240
 Carlberg R.G., et al., 1997, *ApJ*, 476, L7
 Cash J.R., Karp A.H., 1990, *ACM Transactions on Mathematical Software*, 16, 201
 Contini E., De Lucia G., Borgani S., 2012, *MNRAS* 420, 2978
 Conroy C., Wechsler R. H., Kravtsov A. V., 2006, *ApJ*, 647, 201
 Conroy C., Wechsler R. H., 2009, *ApJ*, 696, 620
 De Lucia G., Kauffmann G., Springel V., White S. D. M., Lanzoni B., Stoehr F., Tormen G., Yoshida N., 2004, *MNRAS*, 348, 333
 den Hartog R., Katgert P., 1996, *MNRAS*, 279, 349
 Diemand J., Moore B., Stadel J., 2004, *MNRAS*, 352, 535
 Domínguez M.J., Zandivarez A.A., Martínez H.J., Merchán M.E., Muriel H., Lambas D.G., 2002, *ApJ*, 335, 825
 Dutton A.A., van den Bosch F.C., 2012, *MNRAS*, 421, 608
 Faltenbacher A., Diemand J., 2006, *MNRAS*, 369, 1698
 Faltenbacher A., Jing Y.P., Li C., Mao S., Mo H.J., Pasquali A., van den Bosch F.C., 2008, *ApJ*, 675, 146
 Gao L., White S. D. M., Jenkins A., Stoehr F., Springel V., 2004, *MNRAS*, 355, 819
 Ghigna S., Moore B., Governato F., Lake G., Quinn T., Stadel J., 1998, *MNRAS*, 300, 146
 Ghigna S., Moore B., Governato F., Lake G., Quinn T., Stadel J., 2000, *ApJ*, 544, 616
 Gill S.P.D., Knebe A., Gibson B.K., 2005, *MNRAS*, 356, 1327
 Giocoli C., Tormen G., van den Bosch F.C., 2008, *MNRAS*, 386, 2135
 Giocoli C., Tormen G., Sheth R.K., van den Bosch F.C., 2010, *MNRAS*, 404, 502
 Girardi M., Rigoni E., Mardirossian F., Mezzetti M., 2003, *A&A*, 406, 403
 Gómez P.L., et al., 2003, *ApJ*, 584, 210
 Goto T., Yamauchi C., Fujita Y., Okamura S., Sekiguchi M., Smail I., Bernardi M., Gomez P.L., 2003, *MNRAS*, 346, 601
 Goto T., Yagi M., Tanaka M., Okamura S., 2004, *MNRAS*, 348, 515
 Guo Q., White S., Li C., Boylan-Kolchin M., 2010, *MNRAS*, 404, 1111
 Hearin A.P., Watson D.F., 2013, *MNRAS*, 432, 1313
 Hearin A.P., Watson D.F., Becker M.R., Reyes R., Berlind A.A., Zentner A.R., 2014, *MNRAS*, 444, 729

- Hetznecker H., Burkert A., 2006, MNRAS, 370, 1905
- Hudson M. J., Stevenson J. B., Smith R. J., Wegner G. A., Lucey J. R., Simard L., 2010, MNRAS, 409, 405
- Jiang F., van den Bosch F.C., 2014, MNRAS, (arXiv:1403.6827)
- Jiang L., Cole S., Sawala T., Frenk C.S., 2015, MNRAS, 448, 1674
- Klypin A.A., Trujillo-Gomez S., Primack J.R., 2011, ApJ, 740, 102
- Knebe A., Knollmann S.R., Muldrew S.I., Pearce F.R., Aragon-Calvo M.A., Ascasibar Y., Behroozi P.S., Ceverino D., 2011, MNRAS, 415, 2293
- Knebe A., Pearce F. R., Lux H., Ascasibar Y., Behroozi P. S., Casado J., Moran C. C., Diemand J., 2013, MNRAS, 435, 1618
- Kravtsov A.V., Klypin A.A., Khokhlov A.M., 1997, ApJS, 111, 73
- Kravtsov A. V., Berlind A. A., Wechsler R. H., Klypin A. A., Gottlöber S., Allgood B., Primack J. R., 2004, ApJ, 609, 35
- Kravtsov A., Vikhlinin A., Meshcheryakov A., 2014, preprint(arXiv:1401.7329)
- Kuhlen M., Diemand J., Madau P., 2007, ApJ, 671, 1135
- Lares M., Lambas D.G., Sánchez A.G., 2004, MNRAS, 352, 501
- Ludlow A.D., Navarro J.F., Springel V., Jenkins A., Frenk C.S., Helmi A., 2009, ApJ, 692, 931
- McIntosh D.H., Zabludoff A.I., Rix H.-W., Caldwell N., 2005, ApJ, 619, 193
- Mamon G.A., Sanchis T., Salvador-Solé E., Solanes J.M., 2004, A&A, 414, 445
- Mo H., Mao S., White S.D.M., 1998, MNRAS, 295, 319
- Mo H., van den Bosch F.C., White S.D.M., 2010, Galaxy Formation and Evolution, Cambridge University Press
- Nagai D., Kravtsov A. V., 2005, ApJ, 618, 557
- Navarro J.F., Steinmetz M., 1997, ApJ, 478, 13
- Navarro J.F., Frenk C.S., White S.D.M., 1997, ApJ, 490, 493
- Onions J., et al., 2013, MNRAS 429, 2739
- Peebles P.J.E., 1969, ApJ, 155, 393
- Pereira M.J., Bryan G.L., Gill S.P.D., 2008, ApJ, 672, 825
- Planck Collaboration, 2015, preprint (arXiv:1502.01589)
- Postman M. Geller M.J., 1984, ApJ, 281, 95
- Pracy M. B., Driver S. P., De Propriis R., Couch W. J., Nulsen P. E. J., 2005, MNRAS, 364, 1147
- Presotto V. et al., 2012, A&A, 539, A55
- Press W.H., Teukolsky S.A., Vetterling W.T., Flannery B.P., 1992, in Numerical recipes in FORTRAN. The art of scientific computing, Cambridge: University Press
- Quintana H., 1979, AJ, 84, 15
- Reddick R.M., Wechsler R.H., Tinker J.L., Behroozi P.S., 2013, ApJ, 771, 30
- Reed D., Governato F., Quinn T. Gardner J., Stadel J., Lake G., 2005, MNRAS, 359, 1537
- Roberts I.D., Parker L.C., Joshi G.D., Evans F.A., 2015, MNRAS, 448, L1
- Rodríguez-Puebla A., Drory N., Avila-Reese V., 2012, ApJ, 756, 2
- Rood H.J., Turnrose B.E., 1968, ApJ, 152, 1057
- Sales L.V., Navarro J.F., Abadi M.G., Steinmetz, M., 2007, MNRAS, 379, 1475
- Springel V., 2005, MNRAS, 364, 1105
- Springel V. et al., 2008, MNRAS, 391, 1685
- Teyssier M., Johnston K.V., Kuhlen M., 2012, MNRAS, 426, 1808
- Trujillo-Gomez S., Klypin A., Primack J., Romanowsky A.R., 2011, ApJ, 742, 16
- Vale A., Ostriker J. P., 2004, MNRAS, 353, 189
- Vale A., Ostriker J. P., 2006, MNRAS, 371, 1173
- van den Bosch F.C., 2002, MNRAS, 331, 98 (vdB02)
- van den Bosch F.C., Lewis G.F., Lake G., Stadel J., 1999, ApJ, 515, 50
- van den Bosch F.C., Abel T., Croft R.A.C., Hernquist L., White S.D.M., 2002, ApJ, 576, 21
- van den Bosch F.C., Tormen G., Giocoli C., 2005, MNRAS, 359, 1029
- van den Bosch F.C., Pasquali A., Yang X., Mo H.J., Weinmann S., McIntosh D.H., Aquino D., 2008, preprint (arXiv:0805.0002)
- van den Bosch, F.C., Jiang F., 2014, preprint (arXiv:1403.6835)
- van den Bosch, F.C., Jiang F., Hearin A., Campbell D., Watson D., Padmanabhan N., 2014, MNRAS, 445, 1713
- von der Linden A., Wild V., Kauffmann G., White S. D. M., Weinmann S., 2010, MNRAS, 404, 1231
- Vulcani B. et al., 2013, A&A, 550, A58
- Watson D.F., et al., 2015, MNRAS, 446, 651
- Weinmann S.M., van den Bosch F.C., Yang X., Mo H.J., 2006, MNRAS, 366, 2
- Wetzel A.R., 2011, MNRAS, 412, 49
- Wetzel A.R., Tinker J.L., Conroy C., 2012, MNRAS, 424, 232
- Wetzel A.R., Tinker J.L., Conroy C., van den Bosch F.C., 2014, MNRAS, 439, 2687
- Whitmore B.C., Gilmore D.M., Jones C., 1993, ApJ, 407, 489
- Wu H.-Y., Hahn O., Evrard A.E., Wechsler R.H., Dolag K., 2013, MNRAS, 436, 460
- Zentner A. R., Berlind A. A., Bullock J. S., Kravtsov A. V., Wechsler R. H., 2005, ApJ, 624, 505
- Ziparo F. et al., 2013, MNRAS, 434, 3089

APPENDIX A: IMPACT OF SAMPLE SELECTION ON MASS SEGREGATION

In this appendix we take a closer look at how sample selection impacts the results for the segregation of m/M_0 and m_{acc}/M_0 .

The upper panels of Fig. A1 plot the distributions of r/r_{vir} for subhaloes in our fiducial sample, in different bins of m/M_0 (left-hand panel) and m_{acc}/M_0 (right-hand panel). Note that this time we are plotting the full distributions of halo-centric radius, rather than just the averages as in Fig. 3. The thick, grey line indicates the $P(r/r_{\text{vir}})$ distribution for dark matter particles in a NFW halo with a concentration parameter of $c = 10$, and is shown for comparison. Note how subhaloes, independent of their mass, always have a radial distribution that is less centrally concentrated, in good agreement with a number of previous findings (e.g., Ghigna et al. 1998, 2000; Gao et al. 2004; Diemand et al. 2004; Springel et al. 2008).

The color-coding used in the upper panels is indicated in the lower panels, in which the histograms show the distributions of m/M_0 and m_{acc}/M_0 in our fiducial sample. Note that our fiducial sample has no subhaloes with $m_{\text{acc}}/M_0 < -2$. This results in a dramatic drop in the number of subhaloes with $m/M_0 < -2$, which simply reflects that the distribution of m/m_{acc} declines rapidly with increasing m/m_{acc} . Note that whereas m_{acc}/M_0 reveals a monotonic trend of $P(r/r_{\text{vir}})$ shifting to smaller values for increasing m_{acc}/M_0 , the results for m/M_0 are more complicated: for $m/M_0 > 0.01$ the trend is similar to that for m_{acc}/M_0 , with more massive subhaloes having distributions $P(r/r_{\text{vir}})$ that are shifted to smaller values. However, for $m/M_0 < 0.01$ the trend suddenly, and dramatically, reverses. This can be understood as follows. Because of the selection criteria used, subhaloes with $m/M_0 \sim 0.001$ must have $m/m_{\text{acc}} \sim 0.1$. Such subhaloes were typically accreted a long time ago (cf. upper-left panel of Fig. 5), and subhaloes with a large z_{acc} are strongly segregated towards the center of their host.

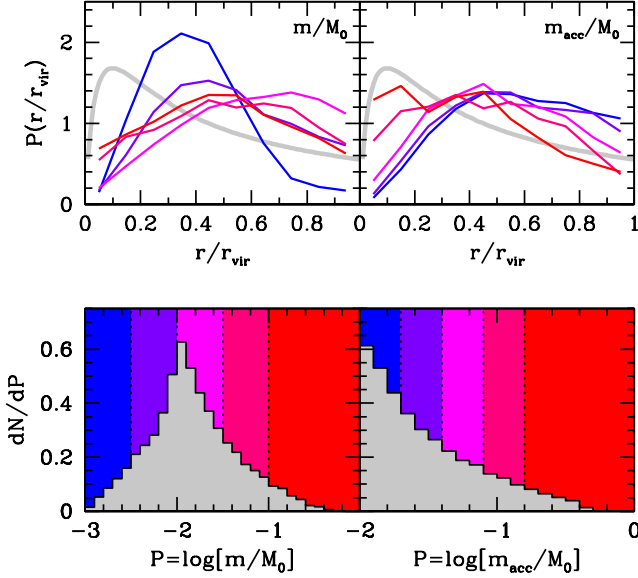


Figure A1. Segregation of subhaloes by present day mass (left-hand panels) and by mass at accretion (right-hand panels). Upper panels show the distributions of r/r_{vir} , with different colors corresponding to different bins in segregation property, as color-coded in the lower row of panels, which also shows the probability distributions of the segregation properties in question. The thick, gray curve in the upper panels corresponds to an NFW profile with a concentration parameter $c = 10$, and is plotted for comparison, to illustrate that the radial distribution of subhaloes is less centrally concentrated than the dark matter.

Fig. A2 is the same as Fig. A1, but now for the enhanced sample, in which we also include subhaloes with $-3 \leq \log[m_{\text{acc}}/M_0] < -2$. This adds the subhaloes in the triangular, pink-shaded region labeled ‘A’ in Fig. 1 and increases the sample size from 66,401 to 291,852 subhaloes. Most of these extra subhaloes have $\log[m_{\text{acc}}/M_0]$ close to -3 . Since our sample is selected to have $\log[m/M_0] \geq -3$, all those subhaloes have m/m_{acc} close to unity, which also means they were accreted very recently. As we have seen in the main text, such subhaloes have low orbital binding energies, on average, and are predominantly located at large halo-centric radii. This explains, then, the dramatic differences that are evident in Fig. A2 with respect to Fig. A1, and illustrates the dramatic impact sample selection can have on the strength and sign of subhalo segregation.

APPENDIX B: THE SPIN STRUCTURE OF DARK MATTER HALOES

As discussed in §4.2, previous studies have argued that stripping matter of a (sub)halo lowers its spin parameter. This is based on the notion that angular momentum is less centrally concentrated than matter. However, it is *inconsistent* with the simulation results of Onions et al. (2013), who measured the spin parameter profile of dark matter subhaloes in simulations, and found $\lambda(< r)$ to *decrease* with increasing radius.

As we show in this Appendix, though, the results of Onions et al. (2013) are an artefact of using poorly resolved haloes. Using haloes that are resolved with of order one mil-

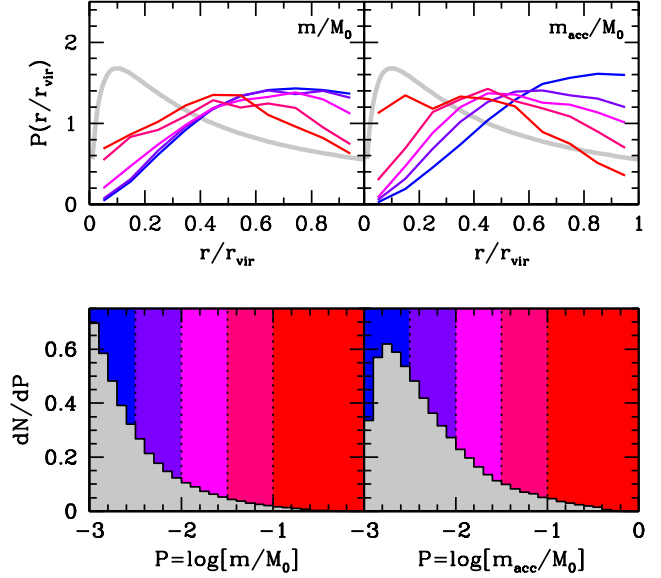


Figure A2. Same as Fig. A1, but this time for the enhanced sample described in the text. Note that $\log[m_{\text{acc}}/M_0]$ now extends down to -3 , and that this time the distributions of r/r_{vir} shift monotonically with changes in m/M_0 or m_{acc}/M_0 .

lion particles each we show that the average $\lambda(< r)$ profile increases with r , but at a remarkably slow rate, and with a huge halo-to-halo variance. However, we start by making a simple analytical prediction for the average spin parameter profile of dark matter haloes.

As shown by Bullock et al. (2001), using high-resolution numerical N -body simulations, the *specific* angular momentum profile of a dark matter halo can be approximated by

$$j(r) \propto [M(< r)]^s \quad (\text{B1})$$

where $s = 1.3 \pm 0.3$. Note, here $j(r)$ is the specific angular momentum *at* radius r , while $M(< r)$ is the mass *inside* of r . We can use this information to predict the spin parameter profile of a dark matter halo. For ease of computation, we adopt here the ‘alternative’ definition for the spin parameter,

$$\lambda' = \frac{J}{\sqrt{2} M r_{\text{vir}} V_{\text{vir}}}, \quad (\text{B2})$$

which was introduced by Bullock et al. (2001), and has the advantage that it does not involve the total energy of the halo. The corresponding spin parameter profile, defined as the spin parameter of the material inside of radius r , can be written as

$$\lambda'(< r) = \frac{1}{\sqrt{2}} \left[\frac{M(< r)}{M} \right]^{-3/2} \frac{J(< r)}{M r_{\text{vir}} V_{\text{vir}}} \quad (\text{B3})$$

where

$$J(< r) = 4\pi \int_0^r j(r) \rho(r) r^2 dr \quad (\text{B4})$$

Using that $j(r) = j_{\text{tot}} [M(< r)/M]^s$, and assuming that dark matter haloes have density profiles that are well approximated by an NFW profile, for which

$$\rho(r) = \frac{M}{4\pi r_s^3 f(c)} \frac{1}{(r/r_s)(1 + r/r_s)^2}. \quad (\text{B5})$$

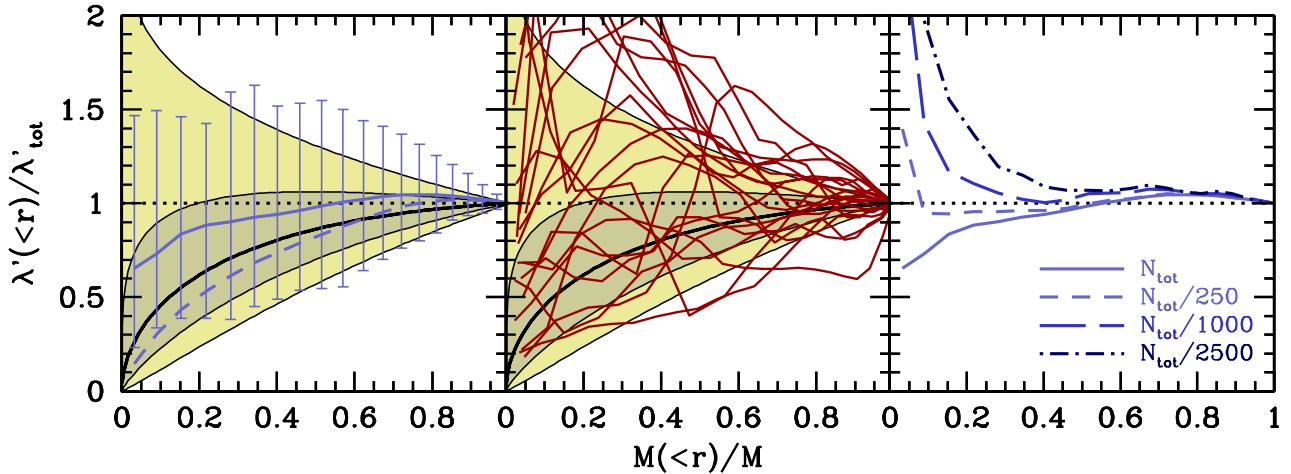


Figure B1. Halo spin parameters of the matter inside radius r , as a function of the mass fraction inside that radius, normalized by the total spin parameter of the halo. The solid, black curve in the middle and left-hand panel are the predictions for the average spin parameter profile for an NFW halo with $c = 5$, while the dark and light yellow shaded regions indicate the expected 1σ and 2σ intervals. The thick, solid blue curve in the left-hand panel is the average spin parameter profile for 228 haloes in the Bolshoi simulation with $10^{14} h^{-1} M_{\odot} \leq M \leq 2 \times 10^{14} h^{-1} M_{\odot}$, with the errorbars indicating the 16 and 84 percentiles of the halo-to-halo variance. The dashed, blue curve is the corresponding spin parameter profile if at each radius the angular momentum vector is projected along the direction of the total angular momentum vector of the halo. The red curves in the middle panel are the spin parameter profiles for a random subset of 20 of the 228 haloes, and clearly show that spin parameter profiles for individual haloes can be very different from their average. Finally, the four curves in the right-hand panel show how the average spin parameter for the 228 haloes (solid line) changes if one downsamples their particles. The short-dashed, long-dashed and dot-dashed curves correspond to the spin parameter profiles obtained when only including randomly one in 250, 1000, and 2500 particles, respectively. See text for a detailed discussion.

with $c = r_{\text{vir}}/r_s$ the NFW concentration parameter and the function $f(x)$ given by Eq. (3), one has that

$$\frac{\lambda'(<r)}{\lambda'_{\text{tot}}} = \left[\frac{f(cx)}{f(c)} \right]^{-3/2} \frac{h(cx)}{h(c)} \frac{1}{\sqrt{x}}. \quad (\text{B6})$$

Here $x = r/r_{\text{vir}}$, $\lambda'_{\text{tot}} = \lambda'(<r_{\text{vir}})$ is the total halo spin parameter, and

$$h(x) = \int_0^x \frac{y [f(y)]^s dy}{(1+y)^2}, \quad (\text{B7})$$

The thick, black, solid line in the left-hand panel of Fig. B1 shows the spin parameter profile $\lambda'(<r)/\lambda'_{\text{tot}}$ as a function of $M(<r)/M$ for $s = 1.3$ and assuming a NFW concentration parameter of $c = 5$, appropriate for massive haloes^{††}. The dark and light yellow shaded regions mark the 68% and 95% confidence regions, and are computed using $s = 1.3 \pm 0.3$ (i.e., the 68% and 95% confidence regions are bounded by $s = [1.0, 1.6]$ and $[0.7, 1.9]$, respectively). Note how the average spin profile increases with enclosed mass, but that the effect is weak; even after stripping off 70 percent of the mass, the spin parameter of the remaining core is only about 20 percent smaller than that of the halo prior to stripping. Note also that the expected halo-to-halo variance is large, and that a significant fraction of subhaloes is expected to have spin profiles that *decrease* with the enclosed mass (or radius).

To test this analytical prediction, we have computed the spin profiles of well-resolved dark matter haloes in the Bolshoi simulation at $z = 0$, using the same method as

in van den Bosch et al. (2002). The solid, blue curve is the average spin parameter profile that we obtained from the 228 dark matter haloes in the Bolshoi simulation with $10^{14} h^{-1} M_{\odot} \leq M \leq 2 \times 10^{14} h^{-1} M_{\odot}$. These haloes contain, on average, close to one million particles per halo, and have an average concentration of ~ 5 . The trend is similar as for our analytical prediction, but the simulation results are somewhat offset to larger $\lambda'(<r)/\lambda'_{\text{tot}}$. This mainly comes from the fact that the $j(r)$ profile measured by Bullock et al. (2001), and used in our analytical derivation, is computed *projected* along the angular momentum axis of the entire halo. Since the direction of $\vec{j}(r)$ can change appreciably with radius (see e.g., Bullock et al. 2001; van den Bosch et al. 2002), our prediction for the radial dependency of the spin profile may have been underestimated. To test the impact of this, the dashed, blue curve in the left-hand panel of Fig. B1 shows the average $\lambda'(<r)/\lambda'_{\text{tot}}$ profile obtained from the same 228 dark matter haloes if we always compute the angular momentum profile of each halo projected in the direction of its total angular momentum vector. This lowers the resulting $\lambda'(<r)/\lambda'_{\text{tot}}$ profile, bringing it in good agreement with our analytical prediction. We emphasize, though, that for the purpose of estimating the impact of mass stripping on the spin parameter, the relevant result is that depicted by the solid, blue curve. This indicates that mass stripping has, on average, very little impact on the spin parameter: even after stripping of 80 percent of the mass, one expects that the remaining remnant has a spin parameter that is roughly 85 percent of that prior to stripping. Note, though, that this ‘prediction’ is only valid if the stripping process itself does not modify the angular momentum profile of the halo, which, as we have argued in §4.2 is unlikely to be the case.

^{††} The dependence on c is fairly weak, with the variance due to scatter in c being subdominant to that due to the scatter in s .

The errorbars in the left-hand panel of Fig. B1 mark the 16 and 84 percentiles of the halo-to-halo variance. Note that this variance is *much* larger than predicted by our ‘model’. This is also illustrated in the middle panel, which plots the actual $\lambda'(< r)/\lambda'_{\text{tot}}$ profiles for a random subset of 20 of the 228 haloes in our sample. Note the dramatic halo-to-halo variance, and the complicated, ‘wiggly’ appearance of the individual curves (cf. Fig. 7 in van den Bosch et al. 2002). Hence, whereas $j(r) \propto [M(< r)]^s$ may provide a reasonable description of the *average* angular momentum profile, it clearly is a poor description of that of *individual* haloes (see also discussion in Bullock et al. 2001).

For completeness, we have also computed the predicted spin profile for the spin parameter definition of Eq. (6). Defining the corresponding spin parameter inside a radius r as

$$\lambda(< r) = \frac{J(< r) |E(< r)|^{1/2}}{G [M(< r)]^{5/2}} \quad (\text{B8})$$

and using that

$$E(< r) = 4\pi \int_0^r \frac{1}{2} \rho(r) V_{\text{circ}}^2(r) r^2 dr \quad (\text{B9})$$

(e.g., Mo, Mao & White 1998), with $V_{\text{circ}}^2(r) = GM(< r)/r$ the circular velocity at radius r , it is straightforward to show that

$$\frac{\lambda(< r)}{\lambda_{\text{tot}}} = \left[\frac{f(cx)}{f(c)} \right]^{-5/2} \frac{h(cx)}{h(c)} \left[\frac{\varepsilon(cx)}{\varepsilon(c)} \right]^{1/2}. \quad (\text{B10})$$

with

$$\varepsilon(x) = \int_0^x \frac{f(y) dy}{(1+y)^2} = \frac{1}{2} - \frac{1}{2(1+x)^2} - \frac{\ln(1+x)}{1+x} \quad (\text{B11})$$

We have verified that these $\lambda(< r)/\lambda_{\text{tot}}$ profiles are similar to $\lambda'(< r)/\lambda'_{\text{tot}}$. Hence, all conclusions derived above for λ' are equally valid for the original spin parameter definition of Peebles (1969). The prediction for the spin parameter profile shown in the upper-left panel of Fig. 5 is computed using Eq. (B10) with a concentration parameter of $c = 15$.

Finally, we address the claim by Onions et al. (2013), that the average spin parameter profile of dark matter subhaloes is a rapidly declining function of radius. As Onions et al. correctly point out, and as has been demonstrated by Bett et al. (2007), one needs at least of order 300 particles to measure a reliable value for the spin parameter. Onions et al. therefore only used subhaloes with $N_p > 300$ in their analysis. However, if one requires at least 300 particles to measure a reliable spin parameter, than one needs many more than 300 particles to measure a reliable spin parameter *profile*. To estimate the impact of particle noise on the measurement of $\lambda'(< r)/\lambda'_{\text{tot}}$ we have repeated the above exercise for the 228 Bolshoi haloes by downsampling their particles. The short-dashed, long-dashed and dot-dashed curves in the right-hand panel of Fig. B1 show the spin parameter profiles obtained when only including randomly one in 250, 1000, and 2500 particles, respectively. This downsampling results in an average number of particles per haloes of 4000, 1000 and 400, respectively. The latter is comparable to what Onions et al. (2013) used when measuring the average spin parameter profile of subhaloes, and dramatically overpredicts $\lambda'(< r)/\lambda'_{\text{tot}}$ at small radii. This shows that the

spin parameter profiles inferred by Onions et al. (2013) are severely impacted by particle noise.

In light of this, the alert reader may worry that our analysis of the spin parameter segregation, which is based on subhaloes with $N_p > 50$, is unreliable. However, in addition to cutting on particle number, we have made a number of additional cuts in selecting our sample (see §2.3 for details). If we remove all subhaloes with $N_p < 300$ from our fiducial sample, we only reduce the actual sample size by 8 percent. Repeating our analysis using this reduced sample yields results that are virtually indistinguishable from those presented in §3. Hence, the segregation of spin parameter is real, and not an artefact arising from the fact that spin parameter measurements are biased high for haloes with $N_p \lesssim 300$.